



# Identifying crystal nucleation mechanisms in a synthetic trachybasalt: a multimodal approach

Stefano Peres<sup>1</sup> · Thomas A. Griffiths<sup>1</sup> · Fabio Colle<sup>2</sup> · Stefano Iannini Lelarge<sup>3</sup> · Matteo Masotta<sup>3,4</sup> · Alessio Pontesilli<sup>5</sup> · Lucia Mancini<sup>6</sup> · Rainer Abart<sup>1</sup>

Received: 8 May 2024 / Accepted: 1 August 2024 / Published online: 20 August 2024  
© The Author(s) 2024

## Abstract

To develop new criteria to distinguish different crystal nucleation mechanisms in silicate melts, we performed crystallization experiments using a synthetic hydrous (2 wt% H<sub>2</sub>O) trachybasalt and combined three-dimensional information from synchrotron X-ray computed microtomography with two-dimensional mapping of crystallographic orientation relationships (CORs) using electron backscatter diffraction. Crystallization experiments were performed at 400 MPa by cooling the melt from 1300 °C to resting temperatures of 1150 and 1100 °C and maintaining isothermal conditions for 30 min and 8 h. Three distinct titanomagnetite (Tmt) populations formed: (1) skeletal crystals, isolated or partially embedded in clinopyroxene (Cpx); (2) anhedral crystals, always attached to Cpx; (3) flattened needle-shaped crystals, embedded in Cpx. These morphologically different Tmt populations formed in response to one cooling event, with varying nucleation mechanisms and at different undercooling conditions. The clustered three-dimensional distribution of population 2 and 3 Tmt grains and the high proportion of Tmt-Cpx interfaces sharing CORs indicate that these Tmt grains heterogeneously nucleated on Cpx. The near-random three-dimensional distribution of (often isolated) population 1 Tmt grains, together with the low proportion of Tmt-Cpx interfaces sharing CORs, imply their isolated, possibly homogeneous nucleation, potentially followed by heterogeneous nucleation of Cpx on population 1 Tmt. Heterogeneous nucleation in slightly to moderately undercooled magmas should affect the sequence of crystallization as well as morphology and clustering of crystals, which may actively contribute to the variation of rheological parameters like viscosity. Finally, observed intra- and inter-sample variations in Tmt-Cpx COR frequencies indicate the potential for this parameter to record further petrological information.

**Keywords** Experimental petrology · Nucleation mechanisms · Heterogeneous nucleation · Crystal clustering · Crystallographic orientation relationships · Microstructural analysis · SR-μCT · EBSD · Trachybasalt

## Introduction

Recent geophysical and volcanological evidence suggests that magma chambers and, on a larger scale, volcanic plumbing systems, are constituted by melt-crystal mixtures known

as crystal mushes (Bachmann and Huber 2016; Cashman et al. 2017), defined as crystal-bearing partially molten systems in which the crystals are arranged in a framework, with melt occupying the remaining space (e.g. Marsh 2002). Furthermore, even at higher melt proportions, magmas almost

Communicated by Dante Canil.

✉ Stefano Peres  
stefano.peres@univie.ac.at

<sup>1</sup> Department of Lithospheric Research, University of Vienna, Josef-Holaubek-Platz 2 (UZA II), Wien 1090, Austria

<sup>2</sup> Dipartimento di Scienze Chimiche, della Vita e della Sostenibilità Ambientale, Università di Parma, Campus Universitario, Parco Area delle Scienze 157A, Parma 43124, Italy

<sup>3</sup> Dipartimento di Scienze della Terra, University of Pisa, Via Santa Maria 53, Pisa 56126, Italy

<sup>4</sup> CISUP, Centro per l'Integrazione della Strumentazione Università di Pisa, Lungarno Pacinotti 43, Pisa 56125, Italy

<sup>5</sup> Istituto Nazionale di Geofisica e Vulcanologia, Via di Vigna Murata 605, Roma 00143, Italy

<sup>6</sup> ZAG–Slovenian National Building and Civil Engineering Institute, Dimičeva ulica 12, Ljubljana 1000, Slovenia

always bear some crystals, whose amount, grain size distribution, and grain shape influence magma rheology and can be modified by clustering processes (e.g. Holness et al. 2017). Therefore, in all magmatic systems, it is of primary importance to understand the interaction between crystals, in particular the formation of rigid aggregates of many individual grains, i.e. crystal clusters. Determining the mechanisms of crystal clustering is pivotal for assessing the evolution of magmatic systems and, via clusters' influence on rheology, their eruptive style.

Crystal clusters composed of relatively few grains have also been referred to as clumps, clots, and glomerocrysts (Garcia and Jacobson 1979; Schwindinger and Anderson 1989; Jerram and Cheadle 2000; Jerram et al. 2003). Here, we define crystal clusters as groups of grains that are joined by areas of grain and/or phase boundary (e.g. Ferguson et al. 2019), formed by crystallization within a magma, or by a disaggregation of a pre-existing crystal mush. Crystal clusters constitute one of the main building blocks from which igneous microstructures develop (Jerram et al. 2003; Holness et al. 2023) and can give information about cooling history (Bachmann et al. 2002), chemical and mechanical magma differentiation (Schwindinger 1999) as well as the physical conditions of crystallization (Hammer et al. 2010; Ellis et al. 2014; Holness et al. 2017, 2019).

Clustering of crystals during crystallization of a magma can occur by three main mechanisms: (a) heterogeneous nucleation, (b) synneusis and (c) passive accumulation. Heterogeneous nucleation occurs when a new crystal nucleates and grows at the interface between the melt and a pre-existing substrate; this mechanism is increasingly favoured with increasing degree of undercooling ( $\Delta T$ ), defined as the difference between the liquidus temperature of a mineral phase ( $T_{liq}$ ) and the effective temperature at which the mineral phase crystallises (Kirkpatrick 1981). Compared to homogeneous nucleation, heterogeneous nucleation is favoured because the creation of a crystal-melt interface would be energetically more expensive than the creation of the same area of crystal-crystal interface. Heterogeneous nucleation is assumed to be the main clustering mechanism occurring in nature and during crystallization experiments (Walker et al. 1976; Lofgren 1983; Hammer 2008; Hammer et al. 2010; Mollo et al. 2012; Arzilli et al. 2015, 2019; Pontesilli et al. 2019; Colle et al. 2023). An important consequence of heterogeneous nucleation is that the appearance of a crystal phase can influence the timing and mechanism of nucleation of another phase, and consequently the order of crystallization in a rock/sample, especially in conditions far from thermodynamic equilibrium (Mollo et al. 2012). Synneusis occurs when two suspended crystals drift together and align during crystal settling or magma flow, typically attaching in preferred orientations that result in a lower interfacial

energy (Vance 1969; Schwindinger 1999; Wieser et al. 2019; DiBenedetto et al. 2020; Dyck and Holness 2021). Finally, passive accumulation of crystals is the final result of settling, with the crystal arrangement determined by the combination of gravitational forces, crystal shape, and fluid dynamics (Rudge et al. 2008).

These clustering mechanisms are often inferred on the basis of microstructural observations. Perpendicular projection of elongate crystals from an interface in the direction of the melt has been invoked as evidence of heterogeneous nucleation (Kirkpatrick 1977; Hammer et al. 2010; Arzilli et al. 2015; Vetere et al. 2015; Colle et al. 2023). The offset of the true centres of clustered, concentrically zoned crystals from the mutual boundary has been invoked as evidence for synneusis (Vance 1969; Dowty 1980). Shape preferred orientation (SPO) in the form of magmatic foliation or lineation of minerals, and/or poikilitic and adcumulate microstructures are some of the microstructural evidence for accumulation processes (Holness et al. 2017, 2023; and references therein).

To date, only a limited number of studies have provided crystallographic evidence in support of their interpretation of clustering mechanism. Variable crystallographic orientation relationships (CORs, Habler and Griffiths 2017) can be observed in crystal clusters formed either by heterogeneous nucleation (e.g. Hammer et al. 2010) or synneusis (e.g. Wieser et al. 2019; Dyck 2023; Gordon and Wallis 2024). These two clustering mechanisms differ in the degree of freedom allowed in the relationship between the lattices of the touching phases, and thus, in the characteristics of the CORs formed. During heterogeneous nucleation, the lattice of the pre-existing crystal should guide the nucleation and growth of the new phase in a highly restricted orientation, in order to minimize misfit with the newly formed lattice (Holness et al. 2023 and references therein). In synneusis, facets of already formed crystals come in contact, allowing small rotations of the lattices perpendicular to the interfaces and small deviations from exact parallelism of facets.

Regarding rocks formed by passive accumulation, CORs have never been studied. Indeed, if the accumulated crystals show no SPO or CPO (Wieser et al. 2019; Holness et al. 2023), certainly CORs are also absent. In contrast, strongly foliated or lineated cumulates may also be characterized by a CPO (e.g. Holness et al. 2017; Vukmanovic et al. 2018; Bertollett et al. 2019). Consequently, CORs might develop via passive crystal accumulation but should be both “statistical” (Habler and Griffiths 2017) and weak, i.e. exhibit a large degree of freedom in the misorientation between touching crystals.

In this work, we combine synchrotron radiation computed microtomography (SR  $\mu$ CT) with Electron Backscatter Diffraction (EBSD) analysis to study heterogeneous

nucleation mechanisms in a synthetic hydrous (2 wt% H<sub>2</sub>O) trachybasalt melt, crystallized experimentally at 4 kbar and 1100–1150 °C in a piston cylinder apparatus. The phase assemblage produced shows significant clustering and consists of abundant clinopyroxene (Cpx), with subordinate titanomagnetite (Tmt), amphibole (Amph), and vesicles (Ves). We focus on Cpx and Tmt crystals, for which heterogeneous nucleation and epitaxial growth of Tmt on Cpx was first inferred by the EBSD analysis of Hammer et al. (2010). For the first time, we are able to determine the location of particular boundary segments characterized by the COR, and the full misorientation between the two lattices. By combining three-dimensional (3D) microstructural information with high resolution two-dimensional (2D) imaging and mapping of crystal orientation and compositional variations, we are able to constrain: (i) the nucleation mechanisms of three different populations of Tmt and (ii) the relative timing of Tmt formation compared to the appearance of Cpx crystals. We show that the combination of EBSD with 3D X-ray imaging by SR  $\mu$ CT allows multiple nucleation mechanisms to be distinguished for the same phase during the same cooling event, and furthermore, that multiple crystal morphologies may arise from a single cooling event.

## Methods

### Crystallization experiments

Crystallization experiments were performed using as starting material a trachybasaltic glass, synthesized targeting the chemical composition of the Monte Maletto Formation of Mt. Etna (Italy) (Armienti et al. 1988, 2013). The starting mixture was prepared using analytical grade reagents (Masotta et al. 2020) mixed in stoichiometric proportions. The reagent mixture was put in a ceramic crucible and slowly heated to 1100 °C (for 12 h) to allow complete dehydration and decarbonation. In a second step, the mixture was loaded in a Pt crucible pre-saturated with Fe and left at 1600 °C for 1 h to form a homogeneous melt, then quenched to a crystal-free glass by dropping the crucible into a tank of deionised water. A representative portion of the synthetic glass was analysed by using electron probe microanalysis (EPMA) to check for component loss and chemical homogeneity, as well as to confirm the absence of residual unmelted crystals. The synthetic glass produced had the following composition: SiO<sub>2</sub> = 47.00 ± 0.19 wt%, TiO<sub>2</sub> = 1.72 ± 0.03 wt%, Al<sub>2</sub>O<sub>3</sub> = 15.7 ± 0.19 wt%, FeO = 10.60 ± 0.09 wt%, MgO = 8.38 ± 0.10 wt%, CaO = 12.17 ± 0.13 wt%, Na<sub>2</sub>O = 3.10 ± 0.06 wt%, K<sub>2</sub>O = 1.30 ± 0.04 wt%.

The experiments were carried out in a non-end loaded piston cylinder (QUICKpress) installed at the HP-HT

laboratory of Dipartimento di Scienze della Terra of the University of Pisa (Italy), using a standard 19–25 mm NaCl-pyrex-graphite-MgO assembly. The assembly materials impose oxygen fugacity conditions corresponding to 2 log units above the Ni-NiO buffer (Masotta et al. 2012a). Pt capsules were loaded with the powdered starting glass and nominally 2 wt% of deionised H<sub>2</sub>O (added using a micro syringe), before being welded shut and eventually inspected for weight loss after heating at 110 °C in an oven. Pyrophyllite was used as supporting medium around the capsule in order to prevent H<sub>2</sub>O loss (Freda et al. 2008). The length of the capsules (8 mm) and their position in the assembly were chosen in order to take advantage of the intrinsic temperature gradient of the graphite furnace (as determined by an earlier calibration of the temperature distribution in the furnace and previous experimental work done with the same apparatus; Masotta et al. 2012b; Costa et al. 2020). The temperature gradient imposes at the top of the capsule a temperature that is about 50–60 °C lower than at the bottom, where temperature is measured with a factory calibrated C-type thermocouple (yielding a precision of ± 3 °C). In each experiment, the assembly was cold pressurized to 400 MPa and heated at a rate of 80 °C/min to reach the temperature of 1300 °C. The experiment was maintained at this temperature for 30 min to ensure full melting of the starting glass powder and subsequent melt relaxation, before cooling (at the same rate of 80 °C/min) to the final resting temperatures (T<sub>rest</sub>) of 1150 and 1100 °C. The T<sub>liq</sub> of the trachybasalt with 2 to 3 wt% H<sub>2</sub>O was determined to be 1160–1180 °C based on PhasePlot simulations and previous experimental determination, e.g. Pontesilli et al. 2019; Masotta et al. 2020). Based on the measured length of the capsules after the experiment, we determined the following  $\Delta T$  conditions: (i)  $\Delta T$  varying from 10 °C at the bottom of the capsule to ca. 60 °C at the top for experiments at 1150 °C, and (ii) from 60 °C at the bottom of the capsule to ca. 110 °C at the top for experiments at 1100 °C. Experiments were terminated after 30 min–8 h by turning off the power supply and maintaining the pressure constant during the quench (100 °C/s). Although some experiments were also performed at shorter run durations (dwell time), we discuss the results of three experiments conducted at the following conditions: (a) T<sub>rest</sub> = 1150 °C and 30 min dwell time (abbreviated 1150w-30min), (b) T<sub>rest</sub> = 1100 °C and 30 min dwell time (abbreviated 1100w-30min), (c) T<sub>rest</sub> = 1100 °C and 8 h dwell time (abbreviated 1100w-8h). Sample 1150w-30min was measured by SR  $\mu$ CT only. Unfortunately, during sample preparation for the 2D analysis sample 1150w-30min was lost, preventing further chemical and microstructural analysis. Sample 1100w-30min was analysed through EPMA and EBSD, while sample 1100w-8h was analysed by all the techniques described in this work.

## Synchrotron radiation computed microtomography (SR $\mu$ CT) imaging

Experimental samples 1150w-30min and 1100w-8h were removed from the Pt capsule. The two resulting cylindrical samples (up to 2.5 mm in diameter and 4 mm high) were measured by SR- $\mu$ CT at the SYRMEP beamline (Zandomenighi et al. 2010) of the Elettra synchrotron facility in Basovizza (Trieste, Italy), using a filtered polychromatic X-ray beam (filters=1.5 mm Si plus 1 mm Al corresponding to a mean X-ray beam energy of  $\approx 27$  keV). In order to enhance the visualization of the Cpx phase and accurately determine the morphology of Tmt crystals, we worked in propagation-based phase contrast mode (Polacci et al. 2010). The detector used was a 16-bit, water-cooled, sCMOS macroscope camera (Hamamatsu C11440-22 C) with a 2048 $\times$ 2048 pixel chip coupled, through a high numerical aperture optics, to a 17  $\mu$ m-thick GGG: Eu scintillator screen. Scans were acquired setting a sample-to-detector distance of 175 mm. The scans of the whole samples were acquired in local area mode, scanning separately the upper and lower part of the sample with an effective pixel size of the camera set at 0.9  $\mu$ m (corresponding to a field of view of approx. 1.8 $\times$ 1.8 mm). For each scan 1800 radiographs (projections) of the sample over a total rotation angle of 180 $^\circ$  were acquired with an exposure time per projection of 1.2 s. The SYRMEP Tomo Project (STP) software suite (Brun et al. 2015) was used to reconstruct the imaged virtual volumes. In order to maximize the quality of the reconstruction and optimize the visibility of the different phases of interest, a single-distance phase retrieval algorithm (Paganin et al. 2002) was applied to projections prior to tomographic reconstruction setting the delta/beta parameter (ratio between the real and imaginary parts of the X-ray refraction index of the material) to 17. The STP software was used also for ring artefact correction.

## EPMA

Cpx, Tmt, Amph and glass major element analyses and chemical maps were performed at the Department of Lithospheric Research of the University of Vienna, Austria, using a CAMECA SXFiveFE EPMA equipped with five wavelength dispersive spectrometers and one energy-dispersive X-ray spectrometer (EDX). All four phases were analysed at 15 kV accelerating voltage and beam current of 20 nA. A beam diameter of 1  $\mu$ m was used for Cpx, Amph and Tmt spot analysis, while a diameter of 5  $\mu$ m was used for the glass analysis. Peak counting times varied for each element: Na=10 s; Si=14 s, Al=10 s; Fe=22 s; K=10 s; Ca=20 s; Mg=20 s; Ti=15 s; Mn=24 s. Detection limits were: 100–250 ppm for Al, Na, Mn, and Ti; 300–500 ppm

for Si, Fe, Mg, Ca and K. Element distribution maps were acquired in beam scan mode, with a 35.5 nA beam current and 15 kV accelerating voltage. Map size varied depending on the investigated microstructure, while a fixed step size of 0.33  $\mu$ m and a dwell time per pixel of 80 ms was applied. Relative Mg, Fe, Ca, Na, and Ti concentrations were mapped using five wavelength dispersive spectrometers set to the corresponding  $K\alpha$  emission wavelengths for each element, while Si and Al concentrations were acquired through EDX. Inside chemical maps, point analyses were acquired and the peak intensity of each element mapped calibrated with the respective quantitative concentration using the *Fiji* software (Schindelin et al. 2012).

## Electron backscatter diffraction (EBSD) measurements

In order to determine the crystallographic orientations of the crystals in representative areas and specific spots of interest on samples, EBSD scans were collected using a FEI Quanta 3D FEG-scanning electron microscope (SEM) equipped with an EDAX Digiview 5 EBSD camera (elevation angle 5 $^\circ$ ), located at the laboratory for field-emission scanning electron microscopy and focused ion beam applications at the Faculty of Geosciences, Geography and Astronomy, University of Vienna (Austria). The OIM Data Collection v7.3.1 software was used for EBSD data acquisition, and OIM Analysis 8.0 for re-indexing. Beam conditions for all EBSD scans were 15 kV accelerating voltage and spot size 1.0 ( $\sim 4$  nA probe current), with a 1 mm SEM aperture, a working distance of 14 mm and a beam incidence angle of 20 $^\circ$ . All scans used an EBSD camera binning of 8 $\times$ 8 pixels, a binned pattern size for Hough transforms of 140 pixels, a Hough  $\theta$  step size of 1 $^\circ$  and a 9 $\times$ 9 convolution mask. Step sizes ranged from 320 nm to 650 nm, always on a hexagonal grid. Tmt was indexed as face-centred cubic, Cpx was indexed as monoclinic (b-setting), using the lattice parameters  $a=9.585$  Å,  $b=8.776$  Å,  $c=5.26$  Å, and  $\beta=106.85^\circ$ , and Amph was indexed as monoclinic (b-setting) using the lattice parameters  $a=9.871$  Å,  $b=18.028$  Å,  $c=5.307$  Å, and  $\beta=105.24^\circ$ . After standardizing confidence index values to the highest for each reconstructed grain using OIM Analysis 8.0, the Matlab toolbox MTEX version 5.6.1 (Bachmann et al. 2010; Hielscher et al. 2010) was used for data processing and plotting. Pixels with confidence index values below 0.1 were classified as not indexed. Grains were then calculated using a misorientation angle threshold of 15 $^\circ$ . EBSD pixels belonging to grains less than 4 pixels in size were removed before recalculating grains with the same misorientation angle threshold to obtain the final datasets used for analysis. Finally, six iterations of smoothing were applied to the boundary traces using the smooth ()



function of MTEX. This does not alter the misorientation at boundary segments.

## Image processing and analysis

The processing of 2D images acquired through optical microscopy or EPMA chemical mapping has been performed through the *Fiji* open source software (Schindelin et al. 2012). Each image obtained was transformed to grey levels (0 is black and 255 is white) and scaled. A 2D median filter was used to remove noise.

The SR- $\mu$ CT reconstructed volumes were processed with the Dragonfly software (version 2020.2 ORS, Canada; non-commercial license for academic use). A 3D median filter has been firstly applied and then the Wizard tool, which uses a combination of random forest and neural network algorithms to create trainable models capable of segmenting the Cpx, Tmt and vesicles. In the analytical work we focussed on the Tmt crystals. More specifically we separated crystals with different morphologies into three populations using a semi-automatic segmentation, as detailed in chapter “Titanomagnetite clustering parameters”. A single VOI (volumes of interest) of a significant portion of the samples with size  $1100 \times 1100 \times 1840 \mu\text{m}^3$  and  $1090 \times 1090 \times 1440 \mu\text{m}^3$  for sample 1150w-30min and 1100w-8h respectively has been selected to give an overview of the general features of both samples. To increase the representativeness of different regions of each analysed volume, we selected 4 different VOIs for sample with size of  $600 \times 600 \times 600 \mu\text{m}^3$  (sample 1100w-8h) and 3 different VOIs with size  $500 \times 500 \times 500 \mu\text{m}^3$  (sample 1150w-30min). For a meaningful description of the VOI all segmented Tmt crystal with size  $< 8 \mu\text{m}^3$  have been excluded from the quantitative analysis. We also used Dragonfly for 3D visualization of reconstructed and processed images through volume rendering procedures. The segmented volumes were analysed to extract the following parameters for the Tmt crystals: volume size, spatial distribution of the centroids (defined as the arithmetic mean position of all the points in the volume of a geometric figure) and Feret diameters (defined as the distance between the two parallel planes restricting the object perpendicular to that direction).

## Results

### Microstructural features

We describe the microstructural features of the three experiments dividing each experiment in three regions, corresponding to the parts of the capsule at different temperature conditions: (i) the bottom part, corresponding to the region

at higher temperature and minimum  $\Delta T$ , (ii) the middle part, corresponding to the region at intermediate temperature and  $\Delta T$ , and (iii) the top part, corresponding to the region at lower temperature and maximum  $\Delta T$ .

The (hotter) bottom part of experiment 1150w-30min, where  $\Delta T$  conditions of approximately  $10^\circ\text{C}$  are created, is characterized by equant and large ( $> 100 \mu\text{m}$ ) well-faceted skeletal crystals of Tmt (Fig. 1a and c). Moving towards the intermediate part of the capsule, the crystallinity increases, due to the appearance of relatively large ( $> 500 \mu\text{m}$ ) faceted skeletal crystals of Cpx (Fig. 1b). Tmt and Cpx crystals are very frequently observed in contact, with Tmt occurring preferentially at the outer surface of Cpx crystals (Fig. 1c) but also, to a lesser extent, internally between individual crystal branches. In the (colder) upper part of the capsule, characterized by  $\Delta T$  of ca.  $60^\circ\text{C}$ , the crystallinity increases further and both Cpx and Tmt crystals generally decrease in size ( $> 400 \mu\text{m}$  and  $50 \mu\text{m}$ , respectively), although showing crystal morphologies similar to those observed in the middle part of the capsule (Fig. 1b).

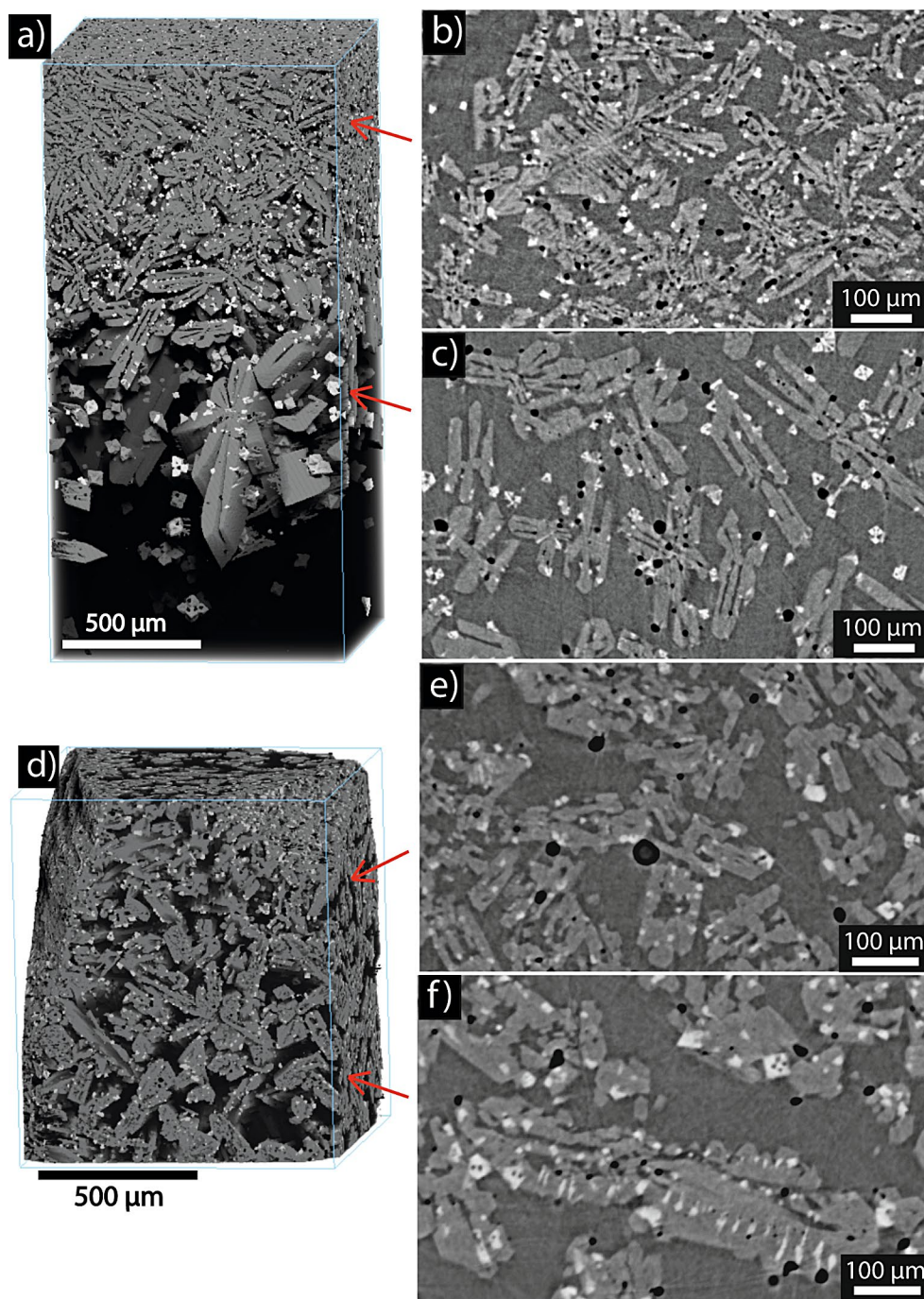
The two experiments performed at  $1100^\circ\text{C}$  (1100w-30min (Supplementary Figure S1) and 1100w-8h, Fig. 1d) produced comparable microstructures: the (hotter) bottom portions of each experiment (Fig. 1f and Supplementary Figure S1c), where  $\Delta T = 60^\circ\text{C}$ , are characterized by large skeletal Cpx crystals up to  $800 \mu\text{m}$  in size and large skeletal Tmt grains up to  $285 \mu\text{m}$ . The Cpx crystals in the 8 h sample are more euhedral compared to the 30 min experiments. The  $1100^\circ\text{C}$  samples also show a slight, but less dramatic, increase in crystallinity from the (hotter) bottom to the (colder) top portion of the sample. The (colder) top parts of these samples, where  $\Delta T$  is ca.  $110^\circ\text{C}$ , are characterized by higher number of smaller ( $100\text{--}300 \mu\text{m}$ ), more dendritic Cpx and smaller anhedral Tmt ( $< 50 \mu\text{m}$ ), always in contact with Cpx grains (Fig. 1e and Supplementary Figure S1d).

### Titanomagnetite populations

Image analysis from synchrotron radiation  $\mu$ CT scans allowed a precise and complete reconstruction of Tmt crystals in samples 1150w-30min and 1100w-8h in 3D. In spite of the different experimental conditions, three populations of Tmt can be distinguished in all samples, based on the dominant crystal habit and microstructural relationship with Cpx:

Population 1 (Skeletal, isolated or not completely embedded in Cpx) Population 1 crystals have skeletal habitus with well-defined external facets, characterized by six skeletal branches disposed in an octahedral arrangement. Skeletal Tmt crystals are mostly equidimensional (Fig. 2a-b) and can reach sizes up to  $285 \mu\text{m}$  (maximum

**Fig. 1** (a) and (d) volume rendering of representative VOIs in the experimental samples 1150w-30min (VOI size:  $1100 \times 1100 \times 1840 \mu\text{m}$ ) and 1100w-8h (VOI size:  $1090 \times 1090 \times 1440 \mu\text{m}$ ) respectively. Voxel size is  $0.9 \mu\text{m}$ . Cpx grains are grey; Tmt grains are light grey; Vesicles are dark grey; glass is translucent. Figure 1b and c are reconstructed slices after image processing from the top and central portions of sample 1150w-30min, respectively. Figure 1e and f are reconstructed slices after image processing from the top and bottom portions of sample 1100w-8h, respectively

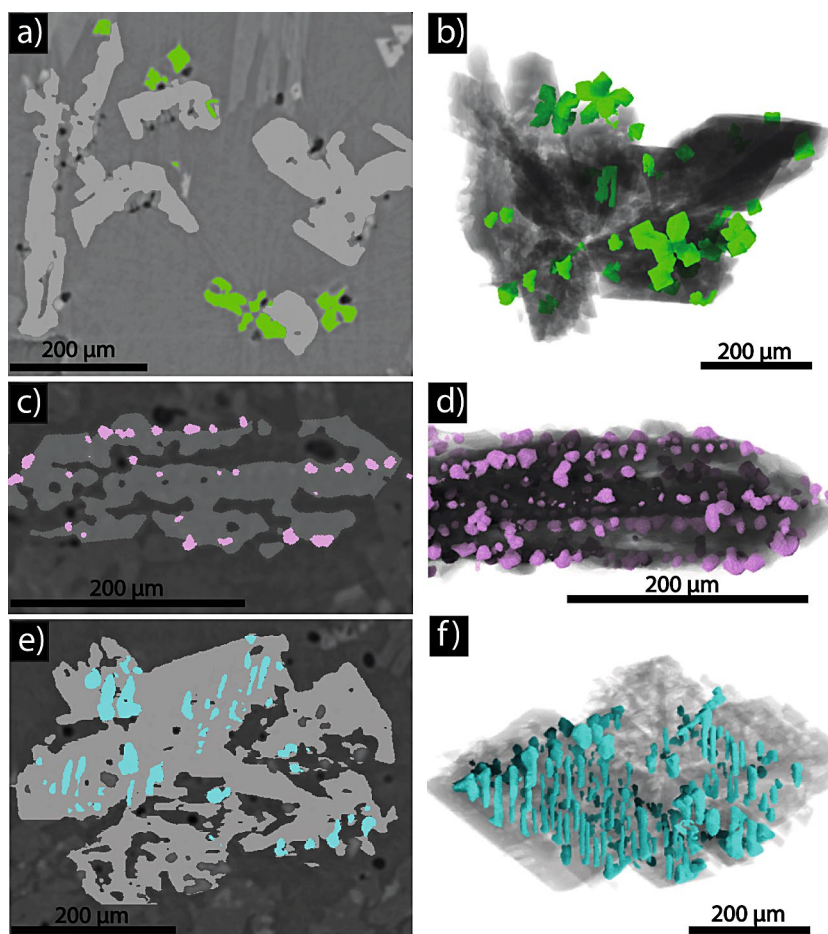


Feret diameter calculated by Dragonfly software). They are larger than the Tmt grains of the other populations at the same location in each capsule. When Tmt crystals of population 1 touch Cpx grains the complete six-branched skeletal Tmt morphology is preserved even when partially or fully embedded inside a Cpx. However, in some cases the central portions of population 1 Tmt grains are in contact with a Cpx, and they show the formation of just 4 or 5 of the crystal branches, lacking

the branch (or branches) that should extend in the direction of the touching Cpx crystal.

**Population 2 (Anhedral, attached to Cpx)** Anhedral Tmt crystals of this population are the most abundant in terms of number and total volume, in all three samples (Fig. 2c-d). The size of the crystals comprising this population varies between  $2 \mu\text{m}$  and  $100 \mu\text{m}$ , and they typically represent the smallest Tmt grains at a given position in each capsule. It is worth noting that all Tmt grains of this population are in contact with a Cpx

**Fig. 2** Three different Tmt populations found in all three experimental runs; in the left column are the reconstructed slices after image processing of Cpx (grey) and Tmt (coloured); in the right column are the 3D rendering pictures of the Tmt grains of the three different populations in the proximity or in contact to the nearest Cpx crystal. (a-b) the green skeletal grains represent Tmt of population 1 (rendered VOI size:  $600 \times 600 \times 315 \mu\text{m}$ ); c-d) the pink anhedral grains represent Tmt of population 2 (rendered VOI size:  $300 \times 200 \times 150 \mu\text{m}$ ); e-f) the cyan elongated grains represent Tmt of population 3 (rendered VOI size:  $450 \times 700 \times 350 \mu\text{m}$ ). Voxel size is  $0.9 \mu\text{m}$



crystal, without being completely embedded. The small, anhedral crystals usually decorate the edges and the tips of larger Cpx crystals, sharing with Cpx a planar or an irregular/rounded interface. In the less-undercooled/hotter portion of the samples, population 2 Tmt grains can also develop a skeletal, externally faceted shape in the direction of the melt outside the Cpx (Fig. 3a-c). Regular spacing in the range between  $10 \mu\text{m}$  and  $30 \mu\text{m}$  is observed between neighbouring population 2 Tmt grains residing on the same Cpx crystal (Figs. 2c-d and 3a-c). A subtype of this population can be identified in samples 1100w-30min and 1150w-30min. These grains are characterized by an elongated shape with max size up to  $100 \mu\text{m}$ , but they are not embedded in the Cpx crystal and, similar to other Tmt grains of population 2, they radiate from the edges or from the exact centre of a dendritic Cpx crystal.

**Population 3 (Flattened needle-shaped crystals, embedded in Cpx)** Flattened needle-shaped Tmt crystals of population 3 are characterized by a high aspect ratio, where the longest dimension (maximum Feret diameter) can reach up to  $120 \mu\text{m}$ , whereas the other two dimensions are in the range between  $10$  and  $50 \mu\text{m}$

(mean Feret diameter) and  $2$  and  $30 \mu\text{m}$  (minimum Feret diameter) (Fig. 4e-f). These flattened needle-shaped crystals are almost completely embedded in Cpx, but they almost always show a melt/Tmt interface at the needle tip. Similar to Tmt population 2, Tmt population 3 also show regular spacing of neighbouring crystals in the range between  $5$  and  $30 \mu\text{m}$  (Figs. 2e-f and 3d-f).

### Clinopyroxene and Titanomagnetite chemistry

BSE images and EPMA data (Fig. 3a, d) show that most Cpx crystals in the two samples are characterized by dendritic zoning, comprising two chemically distinct domains: (1) an  $\text{Al}_2\text{O}_3$ - and  $\text{TiO}_2$ -rich domain (brighter portions of Cpx in BSE [Fig. 3a, d] and  $\text{TiO}_2$  elemental maps [Fig. 3b, e]) and (2) a  $\text{SiO}_2$ - and  $\text{MgO}$ -rich domain (darker portions of Cpx in BSE [Fig. 3a, e], or brighter portions in the  $\text{MgO}$  elemental map [Fig. 3c, f]). In sample 1100w-30min, the  $\text{SiO}_2 + \text{MgO}$  rich zones are only a few  $\mu\text{m}$  thick, comprising thin infillings between bright branches or thin outer rims on Cpx. In sample 1100w-8h, the Cpx crystals are generally larger and the zoning is more pronounced, with  $\text{SiO}_2 + \text{MgO}$



**Fig. 3** (a and d) BSE image of a Cpx showing the typical dendritic sector zoning in sample 1100w-30min and 1100w-8h respectively. b-e and c-f) EPMA microchemical map of the same Cpx crystal showing the relative concentrations of Ti and Mg (c). The grey scale in the image is proportional to the Ti and Mg concentration (black = low, white = high)

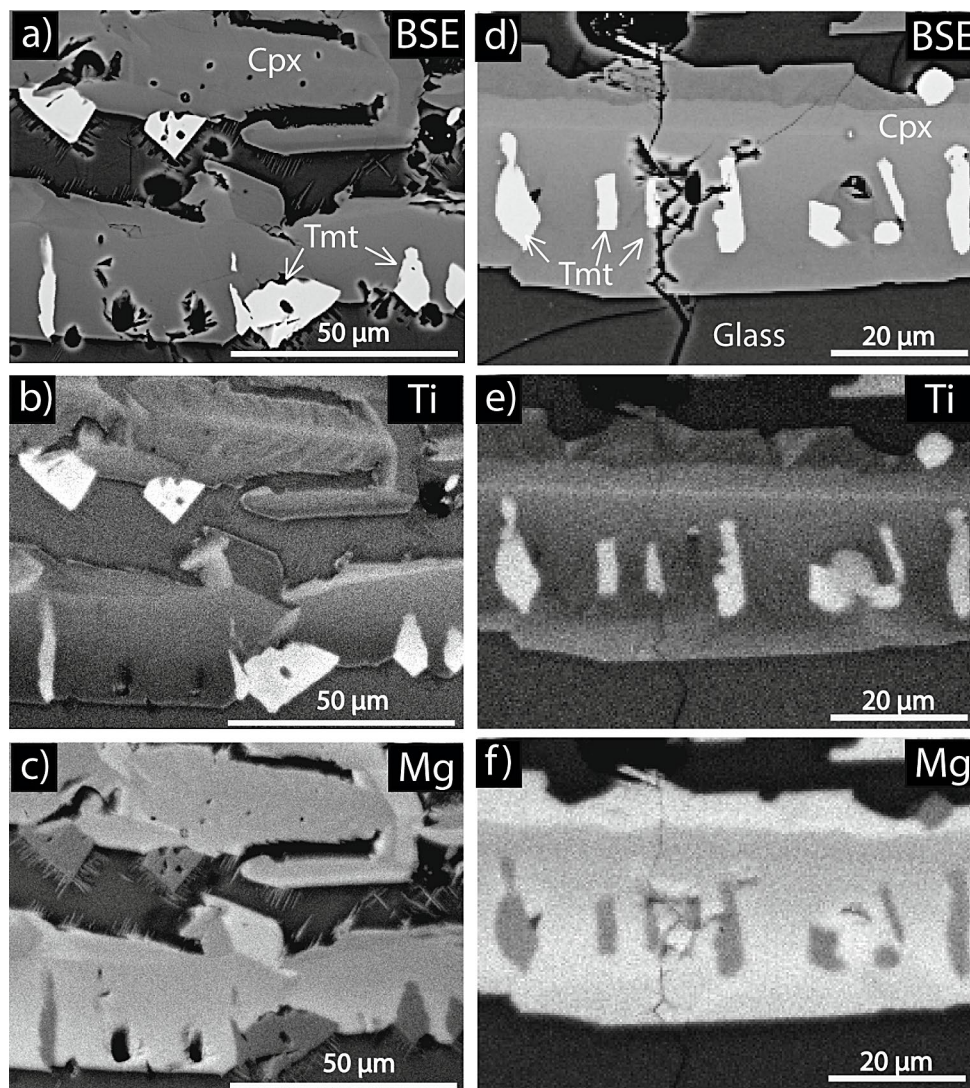
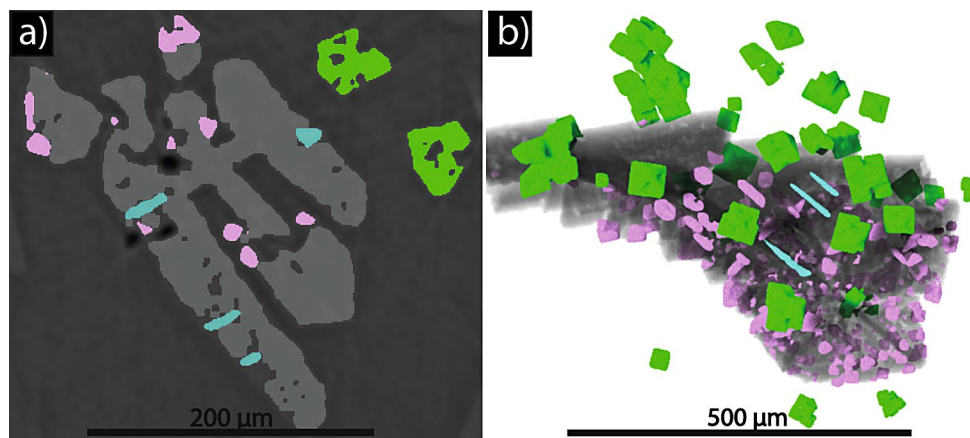


**Fig. 4** (a) reconstructed slice after image processing of Cpx (grey) and Tmt (coloured); (b) 3D rendering of all three different Tmt populations (coloured grains) found next or attached to a single Cpx crystal (light grey) in experimental sample 1100w-8h. (rendered VOI size:  $550 \times 540 \times 600 \mu\text{m}$ ). Voxel size is  $0.9 \mu\text{m}$



rich portions volumetrically more abundant and wider, reaching a few tens of  $\mu\text{m}$  in width. The average compositions of the different zones are reported for the different samples in Table 1.

Spot analyses of single Tmt grains yields oxide compositions from 7.9 wt% to 11.6 wt% MgO, from 8.1 wt% to 12.5 wt%  $\text{Al}_2\text{O}_3$ , from 2.7 wt% to 4.4 wt%  $\text{TiO}_2$  and from 64.5 wt% to 71.5 wt% FeO (Supplementary table,



**Table 1** Chemical compositions of clinopyroxenes in samples 1100w-30min and 1100w-8h

	1100w-30min		1100w-30min		1100w-30min		1100w-8h		1100w-8h		1100w-8h	
	Average (13)	± 1σ	Al+Ti Sect. (11)	± 1σ	Si+Mg Sect. (2)	± 1σ	Average (42)	± 1σ	Al+Ti Sect. (17)	± 1σ	Si+Mg Sect. (25)	± 1σ
SiO <sub>2</sub>	41.58	0.98	41.25	0.64	43.43	0.09	44.67	0.92	41.98	0.92	46.51	0.81
TiO <sub>2</sub>	1.85	0.24	1.91	0.20	1.51	0.08	1.59	0.16	1.82	0.16	1.43	0.20
Al <sub>2</sub> O <sub>3</sub>	10.08	0.85	10.31	0.71	8.81	0.13	8.03	0.66	9.60	0.66	6.97	0.72
FeO <sub>tot</sub>	11.76	0.56	11.85	0.51	11.26	0.54	8.80	0.68	11.24	0.68	7.15	0.49
MgO	11.53	0.68	11.29	0.40	12.84	0.38	12.79	0.58	11.41	0.58	13.73	0.46
CaO	20.33	0.66	20.41	0.53	19.91	1.04	21.97	0.22	21.28	0.22	22.45	0.35
Na <sub>2</sub> O	0.49	0.06	0.51	0.06	0.41	0.03	0.44	0.02	0.45	0.02	0.42	0.02
K <sub>2</sub> O	0.02	0.01	0.02	0.01	0.02	0.01	0.01	0.01	0.01	0.01	0.01	0.01
Total	97.91		98.34		98.34		98.30		97.79		98.67	
<b>Cations per formula unit according to Lindsley and Andersen (1983)</b>												
Si	1.63	0.03	1.62	0.02	1.68	0.00	1.71	0.06	1.64	0.03	1.76	0.02
Ti	0.05	0.01	0.06	0.01	0.04	0.00	0.05	0.01	0.05	0.00	0.04	0.01
Al	0.47	0.04	0.48	0.03	0.40	0.01	0.36	0.07	0.44	0.03	0.31	0.03
Fe <sup>3+</sup>	0.20	0.02	0.21	0.02	0.18	0.00	0.15	0.04	0.20	0.02	0.12	0.01
Fe <sup>2+</sup>	0.18	0.01	0.18	0.01	0.18	0.02	0.13	0.03	0.17	0.01	0.11	0.01
Mg	0.67	0.04	0.66	0.02	0.74	0.02	0.73	0.06	0.67	0.03	0.78	0.02
Ca	0.85	0.03	0.86	0.02	0.83	0.04	0.90	0.01	0.89	0.01	0.91	0.01
Na	0.04	0.01	0.04	0.00	0.03	0.00	0.03	0.00	0.03	0.00	0.03	0.00
DiHd	0.18	0.03	0.17	0.02	0.20	0.04	0.12	0.02	0.14	0.01	0.10	0.01
EnFs	0.70	0.04	0.70	0.04	0.70	0.05	0.78	0.03	0.75	0.01	0.80	0.02
Σ-Ts	0.15	0.02	0.15	0.02	0.13	0.00	0.12	0.02	0.14	0.01	0.11	0.02

“Titanomagnetite” sheet). Cation per formula unit (cation sum=3) and end member conversion (based on charge balance) was carried out using the application End Member Generator\_8.0 (Ferracutti et al. 2015). In all the Tmt crystals, recalculated  $\text{Fe}^{3+}$  cations per formula unit range between 1.30 and 1.45, while  $\text{Fe}^{2+}$  is between 0.50 and 0.71. In terms of mole proportions of spinel endmembers, magnetite and Mg-Ferrite endmembers each constitute (in almost equal amounts) between 28 mol% and 48 mol%, while spinel and hercynite endmembers constitute between 7 mol% and 15 mol%. The mole percentage of Ulvospinel endmember is between 1.6 and 3.0 mol%. No significant difference in composition could be determined between Tmt populations 1 and 2. EPMA chemical maps of population 3 show a clear compositional gradient of increasing  $\text{TiO}_2$  along the crystal long axis. The  $\text{TiO}_2$  content is lower in the portion of Tmt crystals adjacent to the central Al+Ti rich domains of Cpx, and increases towards the outer Si+Mg rich portion of the Cpx crystal. The result is a chemical gradient within Tmt with a similar orientation but opposite in direction compared to the one present in Cpx crystals. In the calibrated map from sample 1100w-8h (“EPMA Maps Calibration”, Supplementary Figure S2 to S6) the inner portions of population 3 Tmt crystals record the lowest amount of  $\text{TiO}_2 = 2.4$  wt%, reaching values of  $\text{TiO}_2 = 3.4$  wt% in the outermost portion of the Tmt. This  $\text{TiO}_2$  is similar to the average  $\text{TiO}_2$  contents measured in of population 2 crystals in the sample.

### Titanomagnetite clustering parameters

We analysed the distribution of Tmt crystal centroids in the 3D domain for samples 1150w-30min and 1100w-8h to verify the presence of periodicities in the distances between adjacent Tmt crystals. Sample 1100w-30min will not be considered since we do not have a 3D scan of the sample and the 2D analysis of the Tmt centroid distribution is not directly comparable to 3D analysis due to cutting effects. The Spatial Point Patterns of Tmt crystal centroids (i.e. the spatial position of only the centroids of the Tmt grains in a volume of interest, abbreviated SPP) in representative volumes of interest (VOIs) reveal whether this phase is statistically clustered, dispersed, or randomly distributed inside the VOI. The main clustering parameter used in this work is the pair correlation function (or radial distribution function)  $g(r)$  (abbreviated pcf from now on), defined by Ripley (1976, 1977) as

$$g(r) = \frac{1}{2\pi r} \frac{dK(r)}{dr} \quad (1)$$

$$\text{where } K(r) = \frac{E}{\lambda} \quad (2)$$

where  $E$  is the number of extra points within radius  $r$  of a randomly chosen point,  $\lambda$  is the intensity (points per unit volume), and  $r$  is the interpoint distance.  $g(r)$  is the probability density function for interpoint distances  $r$ , where  $g(r)=1$  represents complete spatial randomness of a SPP. If  $g(r) > 1$  at a certain  $r$ , then that interpoint distance occurs more frequently than expected for a completely random distribution, indicating clustering (Rudge et al. 2008). Likewise, if  $g(r) < 1$ , that interpoint distance is less frequent than expected for a complete random distribution, indicating ordering. The greater the divergence of  $g(r)$  from 1, the stronger the divergence from a random distribution. The pair correlation function has been analysed using the “pcf” function present in the package spatstat (v1.64-1; Baddeley et al. 2015) available for R software (R Core Team 2020).  $g(r)$  function have been calculated considering both translation and Ripley isotropic edge correction (Stoyan and Stoyan 1994); “trans” and “iso” respectively, in Supplementary table, “pcf” sheet). The results were similar and we decided to show in the relative graphs only  $g(r)$  calculated with Ripley isotropic edge correction.

Pcf values from sample 1150w-30min and 1100w-8h show that for the complete Tmt population, Tmt centroids are overall clustered for interpoint distances between 10  $\mu\text{m}$  and 200  $\mu\text{m}$ , with a peak at interpoint distances between 20  $\mu\text{m}$  and 24  $\mu\text{m}$  reaching a value of  $g(r) = 1.4$ . At interpoint distances greater than 100  $\mu\text{m}$  the spatial disposition of centroids shows weak ordering ( $g(r) < 1$ ) or randomness ( $g(r) = 1$ ).

Tmt grains in tomographic data were sorted into three different populations, as defined above, using the Dragonfly software. From now on we use Pop1, Pop2 and Pop3 when referring to the different Tmt populations. First, all Tmt crystals completely surrounded by glass with a volume  $> 16.2 \mu\text{m}^3$  (manually optimised minimum size threshold) were automatically assigned to Pop1 (100% automatic assignment). Tmt grains that touch or are embedded within Cpx but show a similar fully formed skeletal morphology to isolated Tmt crystals, were manually assigned to Pop1 as well (100% manual assignment). Subsequently, highly elongated grains almost completely embedded within Cpx, typically arranged in regular arrays were assigned to Pop3. For each Cpx in a volume, Tmt grains touching the Cpx that showed a high aspect ratio (identified by low sphericity) and specific 3D orientation (sharing a common value of the theta angle parameter that describes the elongation direction of the crystal) were initially automatically assigned to Pop3. This was followed by a visual inspection to manually remove/add specific misclassified grains from/to Pop3

(~50% of the final total of Pop3 grains were manually assigned). Finally, all grains not assigned to Pop1 or Pop3 were then automatically assigned to Pop2 (i.e. anhedral Tmt grains in touch with Cpx).

After segmentation and the sorting of Tmt into the three different populations, we extracted the shape parameters and centroid position of all Tmt grains in the two samples, to evaluate the spatial distribution of the 3D point patterns for each population (Fig. 5). We defined 3 VOIs of  $500 \times 500 \times 500 \mu\text{m}$  for sample 1150w-30min and 4 VOIs of  $600 \times 600 \times 600 \mu\text{m}$  for sample 1100w-8h. Comparing the  $g(r)$  functions of the SPPs of the different populations reveals significant differences in the spatial distribution of Tmt Pop1 compared to Pop2 and Pop3. The Pop1 pcf (Fig. 5a-b) show unclear, weakly clustered patterns in the range between  $20 \mu\text{m}$  and  $300 \mu\text{m}$  with peak values of  $g(r) < 1.3$  in the VOIs of both samples, with the exception of the VOI sampling the colder portion of sample 1150w-30min (green line in Fig. 5, right column). This VOI is characterized by a higher number of small Tmt crystals, completely isolated in the regions of interstitial glass between Cpx crystals, resulting in a  $g(r) > 4$  at interpoint distances between 0 and  $50 \mu\text{m}$ . Pop2 and Pop3 (Fig. 5c-e) instead show clustering between  $15 \mu\text{m}$  and  $\sim 100 \mu\text{m}$  and a peak of clustering at interpoint

distances between  $20 \mu\text{m}$  and  $30 \mu\text{m}$  ( $g(r)$  between 1.1 and 3, and  $> 1.5$  for all but one VOI).

## EBSD results

Multiple EBSD scans were acquired on samples 1100w-30min and 1100w-8h. Using MTEX, we obtained the crystallographic misorientation across each reconstructed boundary segment shared between Cpx and Tmt. CORs were visualized by plotting the distribution of Tmt orientations with respect to the Cpx lattice for all Tmt-Cpx boundary segments. The resulting pole figures (Fig. 6) show a rotational statistical COR (Habler and Griffiths 2017). There are clear maxima corresponding to a specific COR, but also a limited degree of clockwise rotation of Tmt about  $[010]_{\text{Cpx}}$ , leading to a leftward skew of the pole figure maxima that lie in the Cpx (010) plane.

Two Tmt-Cpx CORs are well-known, albeit from Tmt inclusions in Cpx crystals (Fleet et al. 1980; Feinberg et al. 2004; Ageeva et al. 2017): COR 1 ( $[-110]_{\text{Tmt}} \parallel [010]_{\text{Cpx}}$ ,  $[111]_{\text{Tmt}} \parallel (100)^*_{\text{Cpx}}$ ,  $[-1-12]_{\text{Tmt}} \parallel [001]_{\text{Cpx}}$ ) and COR 2 ( $[-110]_{\text{Tmt}} \parallel [010]_{\text{Cpx}}$ ,  $[-1-11]_{\text{Tmt}} \parallel (-101)^*_{\text{Cpx}}$ ,  $[112]_{\text{Tmt}} \parallel [101]_{\text{Cpx}}$ ). Like the COR observed here and the results of Hammer et al. (2010), both feature one Tmt  $< 110 >$  direction

**Fig. 5** Pair correlation function (pcf) patterns for the VOIs from sample 1100w-8h (left column) and for sample 1150w-30min (right column) for the different Tmt populations. Multiple lines in each plot each display the result for a different VOI in the sample. Not all populations were present in all VOIs. In sample 1150w-30min it was not possible to correctly measure pcf value of Tmt pop 3 because they are not frequent enough to perform the calculations. Magenta lines correspond to VOIs from the hotter ( $\Delta T \approx 10^\circ$ - $20^\circ$  and  $\Delta T \approx 60^\circ$ ) portion of the respective samples, Orange and light blue correspond to VOI in the central ( $\Delta T \approx 30^\circ$ - $40^\circ$  and  $\Delta T \approx 70^\circ$ ) and central-colder ( $\Delta T \approx 50^\circ$ - $60^\circ$  and  $\Delta T \approx 70^\circ$ - $90^\circ$  respectively) portions of the respective samples, dark blue corresponds to a VOI in the colder portion of sample 1100w-8h ( $\Delta T \approx 90^\circ$ - $110^\circ$ )

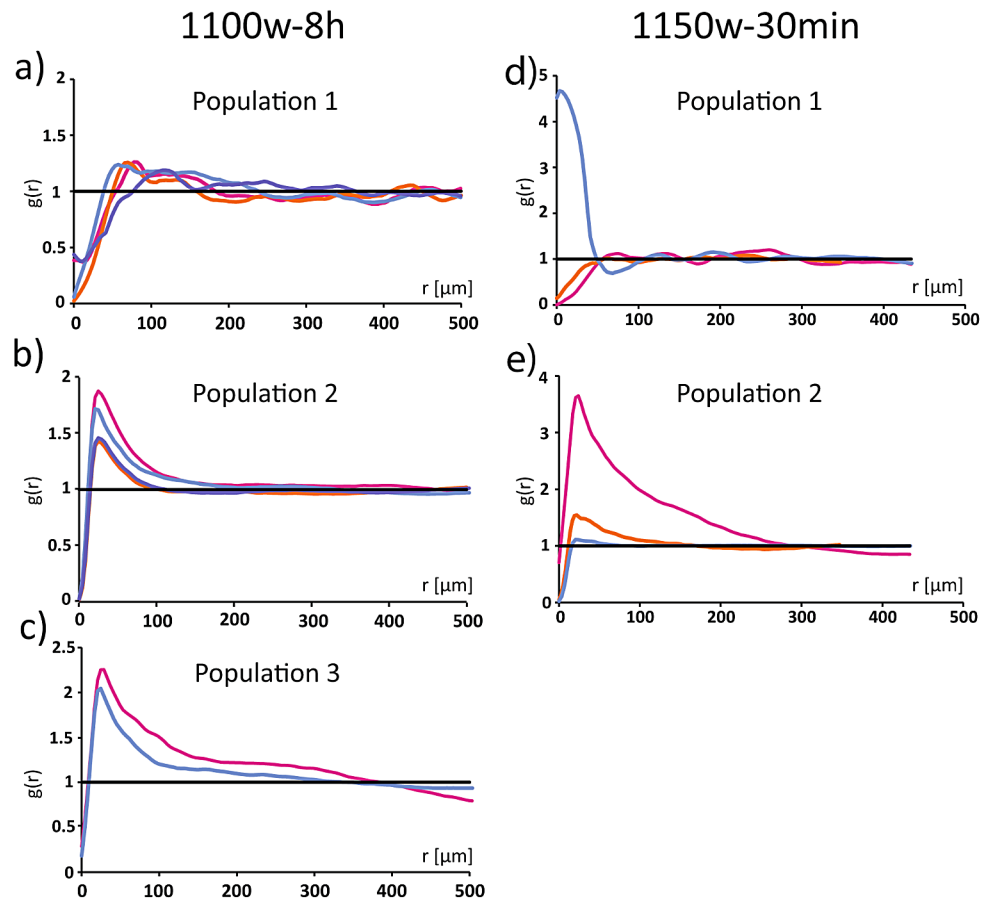
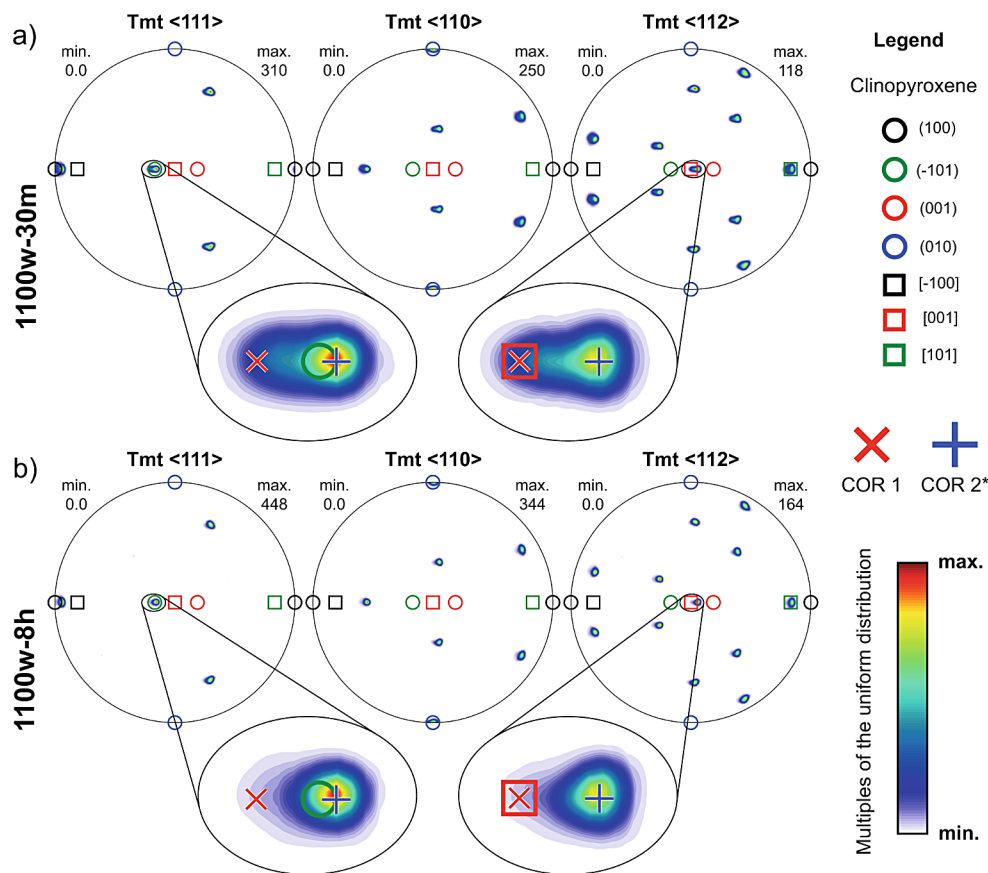




**Fig. 6** Stereographic, upper hemisphere, antipodal pole figures showing the distribution of particular symmetrically equivalent sets of Tmt directions with respect to the lattice of adjacent Cpx for all Tmt-Cpx boundary segments mapped in (a) sample 1100w-30min and (b) sample 1100w-8h. The orientation distribution functions (ODFs) used have a  $1^\circ$  halfwidth (MTEX de la Vallee Poussin kernel). The maximum and minimum intensity is indicated at the top left and right of each pole figure, respectively, in units of multiples of the uniform distribution. The colour map used is shown at right. Important directions (squares) and plane poles (circles) in Cpx are superimposed on all pole figures, colour coded according to the key at right. Zoomed insets of individual maxima are shown, in which the ideal positions of the relevant Tmt plane normal for COR 1 and COR 2\* are marked with a red x or blue +, respectively



parallel to  $[010]_{\text{Cpx}}$ . COR 1 is related to COR 2 by a  $4.3^\circ$  clockwise rotation of Tmt about  $[010]_{\text{Cpx}}$ . Comparing the theoretical misorientations of CORs 1 and 2 to the misorientation distribution in our samples, we find that the misorientation peak in both samples is identical ( $<0.1^\circ$  difference), and differs from the ideal COR 2 by  $1.2^\circ$  (anticlockwise rotation of Tmt about  $[010]_{\text{Cpx}}$ ). We thus designate this commonest Tmt-Cpx boundary misorientation as COR 2\*. The ideal COR 1 corresponds to the maximum extent of the clockwise-skewed orientation distribution, i.e., most Tmt-Cpx boundaries have a misorientation lying between COR 2\* and COR 1 (with a maximum at COR 2\*). The misorientation between COR 2\* and COR 1 is  $5.5^\circ$ .

We classified all Tmt-Cpx boundary segments into one of four categories (Fig. 7): (1) boundary segments with misorientations close to COR 2\* ( $2.7^\circ$  tolerance); (2) boundary segments with misorientations close to COR 1 ( $2.7^\circ$  tolerance); (3) boundary segments not within  $2.7^\circ$  tolerance of COR 1 or COR 2\*, but still with a misorientation  $<6^\circ$  from the midpoint between COR 1 and COR 2\*; and (4) all remaining boundary segments. We then calculated the cumulative boundary length for each category and divided this by the total Tmt-Cpx boundary length, to obtain the boundary length fraction (BLF) belonging to each category, expressed as a percentage, abbreviated below for

the four categories as  $\text{BLF}_{\text{COR1}}$ ,  $\text{BLF}_{\text{COR2}}$ ,  $\text{BLF}_{\text{nearCOR}}$ , and  $\text{BLF}_{\text{noCOR}}$ , respectively. We also calculated the total fraction of boundaries belonging to or adjacent to any COR,  $\text{BLF}_{\text{anyCOR}}$ , as  $100\% - \text{BLF}_{\text{noCOR}}$ .

A total of 2090 and 554 Tmt grains were recognized in EBSD scans of samples 1100w-30min and 1100w-8h respectively, of which 66.7% and 83.8% are in contact (i.e. share a boundary) with a Cpx grain in the 2D scans. Because of 2D cutting problems this value is a great underestimate of the true contact frequency. Image analysis of 3D volumes suggests that the actual proportion of Tmt grains in contact with Cpx is higher than 98% in both samples. Of the total length of Tmt-Cpx boundaries in EBSD scans, 91.0% and 91.1% follow or are close to a COR between Tmt and Cpx, respectively ( $\text{BLF}_{\text{anyCOR}}$ ). This value varies in sample 1100w-30min from 95.3% in the hotter portion of the sample, to 91.1% in the middle and 84.7% in the colder portion of the sample. In contrast,  $\text{BLF}_{\text{anyCOR}}$  in sample 1100w-8h does not show significant variation.

COR 2\* is more prevalent than COR 1 in both samples. Overall,  $\text{BLF}_{\text{COR1}}$  is 20.4% and 6.1% for samples 1100w-30min and 1100w-8h, respectively, while  $\text{BLF}_{\text{COR2}}$  is 51.8% and 72.1% in the same two samples. The relative preferences for the two COR types vary locally throughout both samples.  $\text{BLF}_{\text{COR2}}$  is higher in the hotter portions

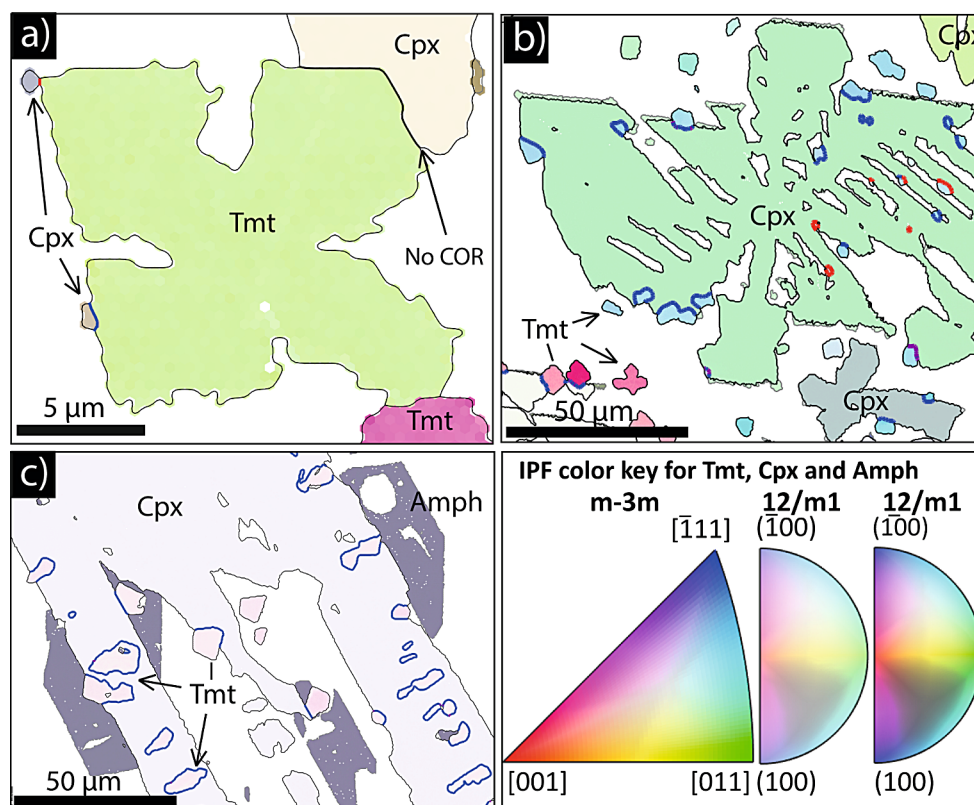


**Fig. 7** EBSD inverse pole figure (IPF) maps of Cpx-Tmt crystal clusters showing different colours for different crystallographic orientations, along with the CORs followed at different Cpx-Tmt boundary segments. **(a)** Population 1 Tmt grain in the bottom portion of sample 1100w-30min, touching a large Cpx grain with no COR (black bold line) and 2 smaller (quench) Cpx grains top left and bottom left, following different CORs with Tmt. **(b)** population 2 Tmt grains (all light blue coloured) touching a single Cpx grain in sample 1100w-30min. Both COR 1 and COR 2\* boundaries are present; **(c)** Population 2

(equidimensional grains) and population 3 (elongated grains) of Tmt in sample 1100w-8h all following COR 2\* with the Cpx grain to which they are attached. *Tmt*=intense colours; *cpx*=lighter colours (60% transparency applied); *Amph*=opaque colours; **Black bold lines**=cpx-tmt interfaces without CORs; **Red bold lines**=cpx-tmt interfaces with COR type 1; **Blue bold lines**=cpx-tmt interfaces with COR type 2\*; **Purple bold lines**=cpx-tmt interfaces outside of COR 1 or COR 2\* but within a range of 6° misorientation

of samples 1100w-30min and 1100w-8h, decreasing from 80.0% to 77.4% in the hotter part down to 34.1% and 58.9% in the cooler part, respectively.  $BLF_{COR1}$ , in an opposite fashion, is at its lowest in the hotter portion, increasing from 5.7% to 1.2% up to 26.8% and 14.5% in the cooler portions of samples 1100w-30min and 1100w-8h, respectively.

In EBSD scans, Tmt populations were sorted by manual visual inspection to identify Tmt Pop1, while to distinguish Pop2 and Pop3 a circularity filter was applied: grains with circularity (defined as short axis / long axis) < 0.4 were classified as Pop3 while grains with circularity > 0.4 were sorted into Pop2. Each Tmt population shows differences in their COR frequencies (Fig. 8). Of all populations, the boundaries of Pop1 grains in contact with a Cpx crystal are characterized by the lowest fraction of CORs, with  $BLF_{noCORs}$  at 17.9% and 33.9% in sample 1100w-30min and 1100w-8h respectively. Moreover, in sample 1100w-8h, Pop1 shows the highest  $BLF_{nearCOR}$  (37.0%). Pop2 is by far the dominant population in both samples, and the Tmt-Cpx boundaries of

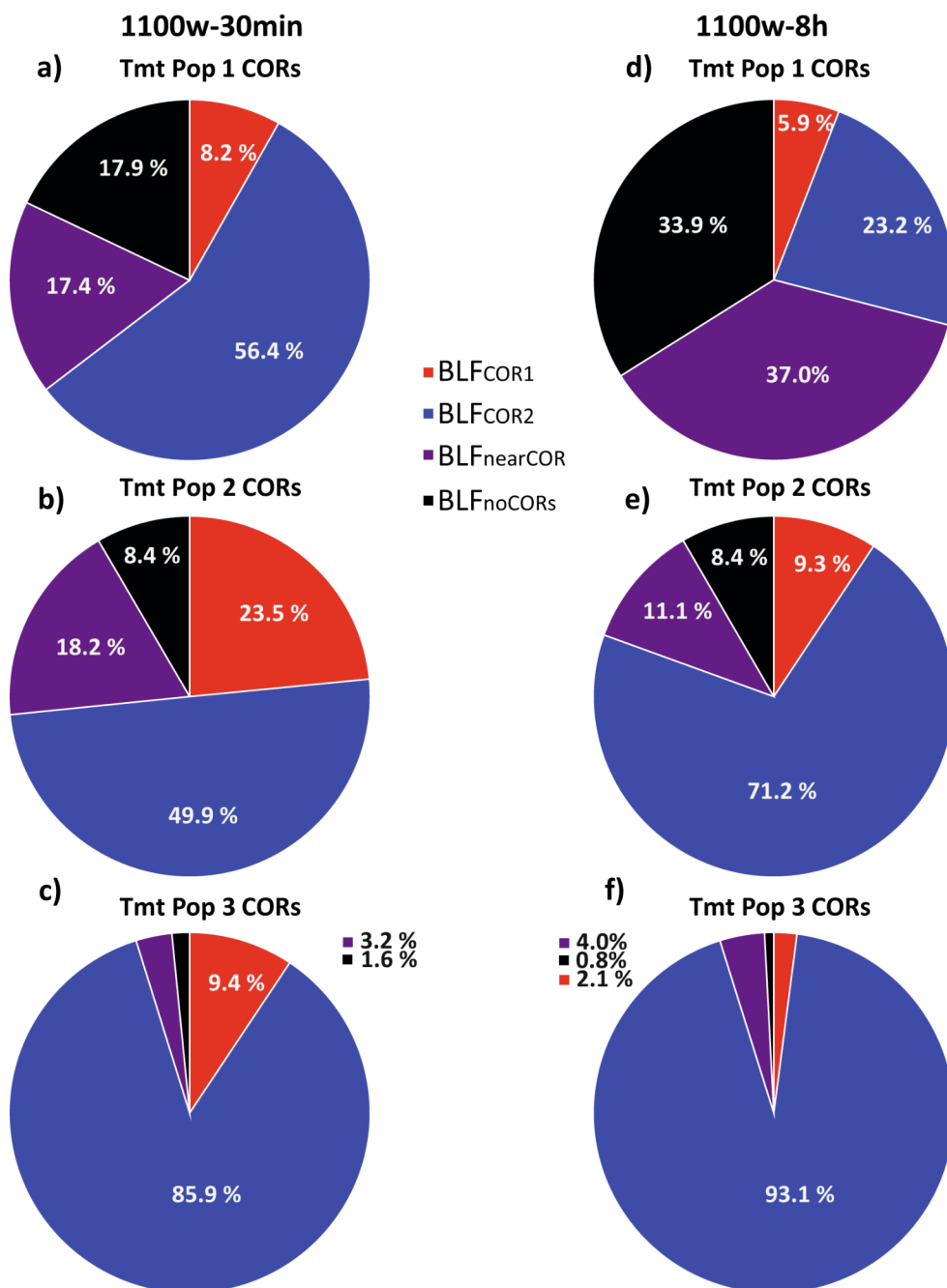
Pop2 are mostly characterized by the presence of COR 2\* ( $BLF_{COR2}$  49.9% and 71.2%, respectively) over COR 1 ( $BLF_{COR1}$  23.5% and 9.3%, respectively). Pop3 grains show the highest  $BLF_{COR2}$  (85.9% and 93.1%, respectively) and as a consequence, the lowest  $BLF_{COR1}$  (9.4% and 2.1%, respectively).

## Discussion

### Nucleation mechanisms of Tmt and Cpx

The presence of three Tmt populations in each sample suggests the occurrence of different nucleation mechanisms and different relative timing of phases' appearance. The diagnostic tools we are going to employ in order to evaluate different nucleation mechanisms are: crystal morphology, spatial relationship of Tmt with the surrounding phases, Tmt clustering parameter  $g(x)$  and Tmt-Cpx CORs.

**Fig. 8** Pie charts of Tmt-Cpx boundary length fraction (in percentages) characterized by CORs in the three Tmt populations in both sample 1100w-30min (left column) and 1100w-8h (right column)



The more likely explanation for Tmt Pop1 grains totally surrounded by glass and isolated from Cpx grains is homogeneous nucleation. However, since our 3D and 2D imaging methodologies cannot resolve objects (like impurities or bubbles) at the nanoscale, it is not possible to exclude that these Tmt grains could have formed by heterogeneous nucleation on undetectable particles. Certainly, for Tmt grains assigned to Pop1 due to their similar size and/or morphology, but partially engulfed in larger Cpx crystals, the recognition of a specific nucleation mechanism requires further evaluation. In sample 1150w-30min, large, skeletal

Tmt grains exhibiting 6 octahedrally arranged branches and well-developed outer facets are the only crystalline phase in the part of the sample with lower  $\Delta T$  (portion of the sample approximately at 1150 °C). We suggest that, due to their similarity with these isolated grains, the engulfed Tmt grains that preserve a skeletal shape and exhibit all 6 octahedral skeletal branches were also formed by the same mechanism (i.e. either homogeneous nucleation from the melt or heterogeneous nucleation on nanoparticles or bubbles), but in any case, prior to their contact with Cpx. Further support for this interpretation is provided by EBSD maps that show



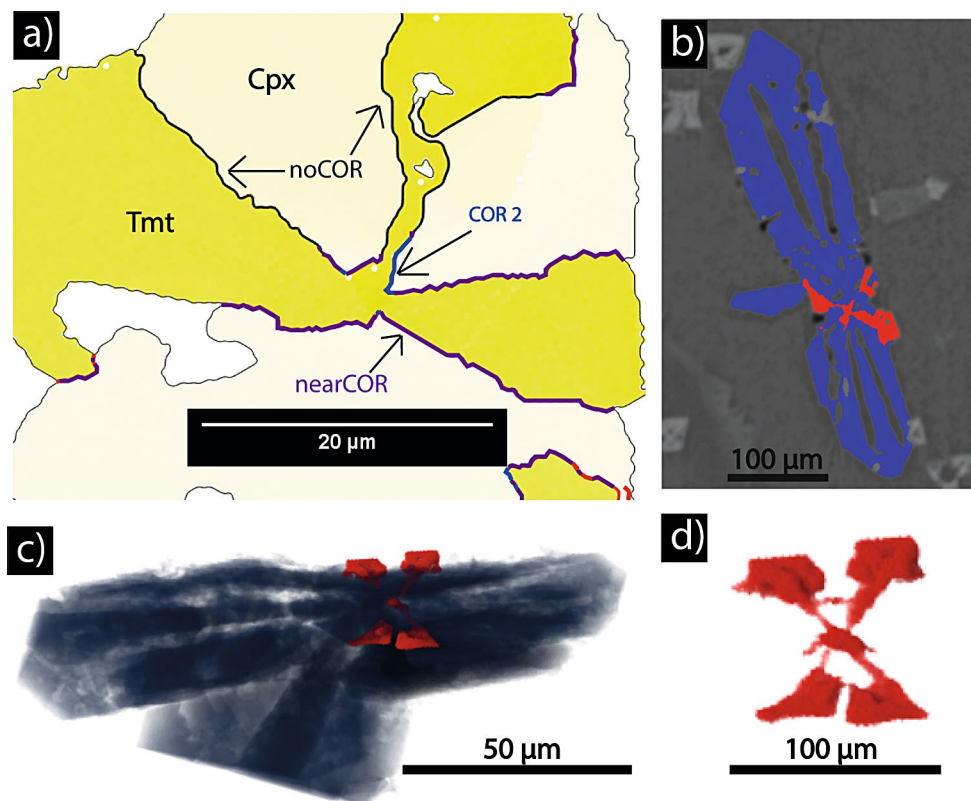
COR-absent boundaries for some Pop1 Tmt grains in touch with Cpx (Fig. 7a). On the other hand, for Tmt grains of Pop1 showing well-formed skeletal shape but missing one or more branches at the contact with Cpx, we suggest that Tmt developed only some of the octahedral branches due to Cpx blocking the extension of other branches into the melt. In EBSD maps where the 2D section is favourably oriented to reveal Tmt grains showing three branches arranged at  $90^\circ$  to each other, with a fourth missing, the inner portion of these Tmt crystals shows the presence of CORs with the adjacent Cpx, whereas the outer facets tend to show no COR (Fig. 9a), suggesting that this morphology developed either due to heterogeneous nucleation of the Tmt grain on Cpx, or vice-versa. A proper distinction of what phase is nucleating on the other is not possible from 2D maps, but these “obstructed” Pop1 Tmt crystals are also observed in our 3D data. In cases where the obstructed Tmt crystal is in contact with the periphery of the Cpx grain, we suggest that heterogeneous nucleation of Tmt on Cpx is more likely. However, some Pop1 Tmt grains are in contact with the central portion of a Cpx grain, from which the Cpx branches radiate (Fig. 9b-d). In such cases, we suggest that Cpx may have heterogeneously nucleated on a pre-existing Tmt at an early stage.

Tmt Pop2 and Pop3 show clear evidence for heterogeneous nucleation on pre-existing Cpx crystals. EBSD scans reveal that Pop2 Tmt grains exhibit a very high length fraction of boundaries shared with Cpx that follow CORs ( $>90\%$

in both samples), and Pop3 boundaries are characterized by an even higher length fraction of CORs ( $>95\%$ ). Heterogeneous nucleation is expected to favour CORs that represent an optimal way of arranging the lattices of crystals at shared interfaces, allowing low-energy interfaces to form, and thus minimising the height of the energetic barrier which governs the likelihood of formation of a stable nucleus. Therefore, it is interesting to know whether the observed CORs indicate the presence of low-energy interfaces. Indeed, the observed CORs represent the case in which one set of  $\{110\}_{\text{Tmt}}$  planes are parallel or at a small angle ( $<2.7^\circ$ ) to the (010) plane of Cpx, and the d-spacings of these planes are similar in both phases (Fleet et al. 1980). In addition, Fleet et al. (1980) showed that, for exactly the two CORs observed here, there is also a correspondence between close packed oxygen planes in Tmt and the arrangement of particular layers of O atoms in Cpx, and furthermore, for the same two CORs, there also exist special (irrational) planes parallel to the  $[010]_{\text{Cpx}}$  direction, along which the structures of Tmt and Cpx should match perfectly. Overall, the overwhelming preference of Tmt-Cpx boundaries for CORs 1 and 2\* in our experiments supports the expectation that the interfacial energies of at least some interface planes associated with these CORs are at a local or global minimum, and provides strong evidence for heterogeneous nucleation.

Despite the fact that interface free energy is dependent on both the misorientation between neighbour crystal lattices as well as on the orientation of the interface plane between

**Fig. 9** (a) EBSD map of a Pop1 Tmt grain from sample 1100w-30min. IPF colour coding is identical to Fig. 8. The grain shows a morphology similar to the one in figures b to d, including an apparent missing branch. (b) reconstructed slice after image processing from sample 1150w-30min and c-d) a 3D rendering of the same crystals from b. These pictures show a cluster of Cpx (blue) and Tmt from Pop1 (red). The peculiar morphology, in which 4 developed Tmt branches out of six possible branches are almost completely engulfed in Cpx in a central position of the Cpx cluster, suggests that the Cpx may have nucleated on the Tmt grain, obstructing the development of the other 2 branches



them, with the interface plane orientation providing the dominant contribution (Habler and Griffiths 2017), we did not find evidence of a preferred interface plane orientation correlating with COR 1 or 2\* boundaries in our EBSD maps. However, we note that the initial interface segment formed during heterogeneous nucleation of a Tmt nucleus on Cpx would be extremely small. In any case, given the frequently observed curved shape of Tmt-Cpx boundary segments with the same COR in our samples, it is clear that after nucleation, the COR did not exert complete control on interface plane orientation. This is in contrast to the observation of Fleet et al. (1980) for exsolved magnetite lamellae, where a different preferred elongation direction was found for each COR. Interestingly, Fleet et al. (1980) observed more needles oriented subparallel to the c-axis of Cpx, corresponding to a preference for COR 1, whereas here, COR 2\* dominates.

In addition to the COR-based evidence for heterogeneous nucleation, we also observed specific preferential interpoint frequencies between 10  $\mu\text{m}$  and 100  $\mu\text{m}$  for both Tmt Pop2 and Pop3, with peaks between 20  $\mu\text{m}$  and 30  $\mu\text{m}$ . This distance range is a good approximation of the average width (minimum axis) of a dendritic Cpx in the region of the sample characterized by higher degrees of  $\Delta T$  (between 60  $^{\circ}\text{C}$  and 110  $^{\circ}\text{C}$ ), or the average width of the single branches of a skeletal Cpx in the (hotter) region characterized by lower degrees of undercooling (between 30  $^{\circ}\text{C}$  and 60  $^{\circ}\text{C}$ ). In this distance range, the diffusion rate of specific elements may play a role in the spacing of neighbour Tmt crystals

nucleating along the same side of a branch, as result of diffusive boundary layers forming at the interface of fast growing Cpx (e.g., Pontesilli et al. 2019). This region is assumed to become supersaturated with respect to Tmt, with the most energetically favourable Tmt nucleation mechanism being heterogeneous nucleation on the growing Cpx crystal. During growth of a newly nucleated Tmt grain, the chemical components that are fractionated into Tmt are depleted in the surrounding melt, lowering their chemical potentials. The extent of depletion of these components in melt around a growing Tmt grain depends on the Tmt growth rate and the diffusivity of the respective components in the melt. Assuming that both the rate of Tmt growth and the component mobilities are quite similar for different Tmt grains within one sample, this produces similarly sized “depletion halos” (domains with reduced chemical potential of the components partitioning into Tmt) around each Tmt grain (Fig. 10). The reduced or absent supersaturation of the melt with respect to Tmt within the depletion halos hinders the nucleation of new Tmt in these domains. By this mechanism, sub-regular spacing of Tmt can be produced along single Cpx facets, as observed.

### Relative timing of nucleation of the different titanomagnetite populations

In this section we discuss the nucleation order of the different Tmt populations and the timing of their nucleation with respect to the development of Cpx crystals, using microstructural relationships and crystal morphologies. In order to interpret the nucleation and growth history of different Tmt populations, it is first important to understand the origin and temporal evolution of the observed Cpx microstructures and zoning. We infer that Cpx may have formed by homogeneous nucleation from the melt, or by heterogeneous nucleation on extremely small particles or bubbles, and/or through heterogeneous nucleation on Pop1 Tmt grains, based on the truncated morphology of some Pop1 Tmt grains and Tmt-Cpx CORs identified near grain centres (Fig. 9). With the exception of the portions of experiment 1150w-30 m characterized by lower undercooling (close to  $T_{\text{liq}}$ ), in the first minutes at the experimental temperature, right after the cooling ramp, the system is far from thermodynamic equilibrium and the melt is supersaturated with respect to Cpx and Tmt (Mollo et al. 2010, 2012, 2013; Pontesilli et al. 2019). Cpx crystallizes in a regime of diffusion-limited crystal growth, so that the growth rate is controlled by the rate at which component diffusion occurs (Sunagawa 1981; Shea and Hammer 2013), eventually resulting in the formation of dendritic crystals characterized by high concentrations of Al + Ti (Fig. 3b-c). As the experimental runs proceed isothermally after reaching the resting temperature, ongoing melt relaxation leads

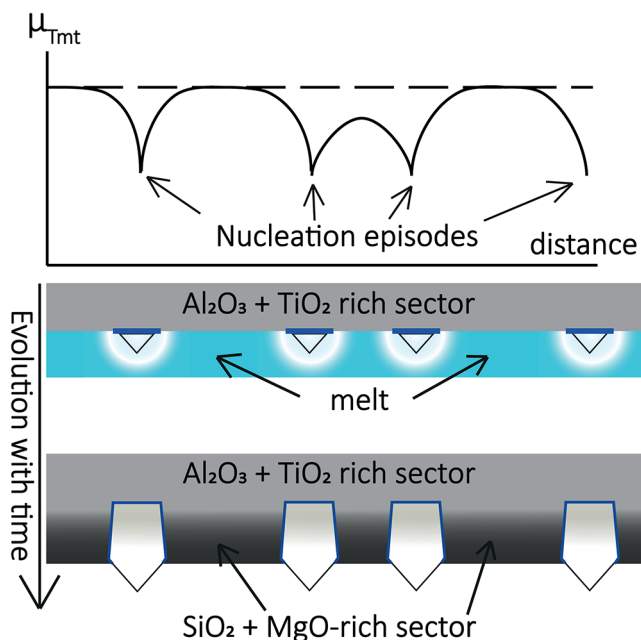


**Fig. 10** Qualitative interpretation of the Tmt chemical potential curve parallel to the Cpx branch after multiple Tmt nucleation episodes. See text for the explanation

to conditions progressively closer to chemical equilibrium, characterized by progressively less supersaturated melt near the crystallizing Cpx, which favours the development of euhedral facets and results in the partial infill of the dendritic branches (Si- and Mg-rich zones; Fig. 3c). In similar experimental samples, Pontesilli et al. (2019) showed that Cpx growth rates decreased in samples kept at experimental temperature for increasing durations between 30 min and 24 h. Thus, we infer that, alongside decreasing melt supersaturation, Cpx growth rates were also decreasing during microstructural evolution of our samples, including during our 30 min duration experiments.

The observation of Tmt (Pop 1) as the liquidus phase (indeed the only crystallizing phase) in the hotter domain of experiment 1150w-30min indicates that Tmt is the first phase to nucleate. The relatively large crystal size and skeletal forms are consistent with the relatively low degree of undercooling determined for this part of the experimental sample (10 °C), as also demonstrated by recent crystallization experiments performed at comparable conditions using a basalt from Stromboli (Colle et al. 2023). Under such conditions of low undercooling, lower nucleation rates and a higher growth rates are expected. In sample 1100w-30min and 1100w-8h, based on well faceted Tmt crystal even when partially engulfed in a Cpx grain and because of the highest amount of shared boundaries between Cpx and Tmt crystals which do not show CORs ( $BLF_{noCORs} = 17.9\%$  and  $33.9\%$ ; Fig. 8a-b) respectively we suggest that, also in these samples, Pop1 Tmt may be the first phase to nucleate.

We infer that Tmt Pop3 nucleated heterogeneously on Cpx in the earlier stages of Cpx growth, favoured by the chemical boundary layer developed at the melt interface. The portion of Pop3 crystals near the  $Al_2O_3 + TiO_2$ -enriched zone of Cpx corresponds to the  $TiO_2$  poor domain of the Tmt crystals, while the  $TiO_2$  concentration increases when the Tmt is situated in the  $SiO_2 + MgO$ -rich zones of Cpx crystals. We suggest that the elongated shape is caused by co-growth of Cpx and Tmt with similar growth rates, resulting in similarity between the Tmt longest dimension and the final width of Cpx branches. Co-growth of the two phases also explains the stronger preference for COR interfaces compared to Pop2 Tmt, as the Tmt-Cpx interface is created simultaneously with the growth of both phases, which favours continued production of a low-energy interface.

Finally, we infer that Pop2 Tmt crystals formed by heterogeneous nucleation on Cpx later in its growth history, when the faceted skeletal morphology of Cpx was more developed, i.e. in conditions closer to thermodynamic equilibrium. This hypothesis is supported by the external position of most Pop2 Tmt grains with respect to touching Cpx, their greater protrusion into the melt, and the presence of frequent planar boundaries between the two crystal phases.

Nonetheless, we in fact observe more or less a continuum of morphologies between the end members which we define as “typical” Pop2 and Pop3 grains (e.g. Figures 3 and 7b-c), and thus many Pop2 Tmt grains exhibit more curved boundaries with Cpx crystals (Figs. 2c, 3a-c and 7b). These can be explained by a slightly earlier timing of Tmt nucleation, possibly corresponding to a limited period of simultaneous growth of the two phases. This would result in a partial embedding of Tmt inside Cpx, with the geometry of the Tmt-Cpx interface controlled by the varying relative growth rates of the two phases in 3D. Despite the existence of transitional forms in between Pop3 and Pop2 morphologies, we still consider it useful to separate Pop3 from the remaining heterogeneously nucleated Tmt grains (Pop2), due to their distinctive morphological, COR, and chemical characteristics. However, the existence of a morphological continuum suggests that heterogeneous nucleation of Tmt on Cpx occurred continuously throughout Cpx growth, i.e., Pop3 and Pop2 do not correspond to separate Tmt nucleation pulses.

## Implications

Our observations show the potential of combining spatially resolved crystallographic orientation maps with high resolution 3D information to provide detailed, spatially resolved petrological information about the conditions and mechanisms of crystal cluster formation. The newly-documented presence of multiple CORs in Cpx-Tmt clusters, whose overall abundance and relative frequency (COR 1 vs. COR 2\*) changes in relation to the degree of undercooling along the experimental sample, suggests that CORs formed by heterogeneous nucleation may represent proxies for deciphering the undercooling conditions in crystal clusters contained in natural magmas. However, it will be essential to carry out further work to understand the reason for the overall higher occurrence of Cpx-Tmt shared boundaries characterized by COR 2\* compared to COR 1, and determine whether this preference is dependent on one or multiple physical parameters.

The second striking feature of our experimental samples is the presence of three different Tmt populations, all of them formed during a single cooling event, nucleated at the same temperature, but at different times, with the only varying condition being the extent of deviation from thermodynamic equilibrium. In the absence of combined 3D analysis and crystallographic orientation information, these different crystal populations of the same phase could have been misinterpreted as evidence of multiple temporally discrete magmatic events. Our results underline the central importance of a multimethodological analysis, not just microstructural observations, in order to explain different populations of the



same crystal phase. In future, the combined application of 3D imaging, compositional mapping, and crystallographic analysis to crystal clusters offers the potential to unravel crystallization sequences with unprecedented (relative) time resolution in experimental samples and natural rocks.

From a broader volcanological point of view, our experiments reproduce magmatic conditions far from equilibrium, which can occur in the context of fast crystallization of a trachybasaltic dike (Arzilli et al. 2022) or crystallization due to a magmatic recharge of trachybasaltic composition in a crystal mush at medium to shallow (10–12 km) depths (Pontesilli et al. 2019; Masotta et al. 2020). The aforementioned works experimentally reproduce crystallization of a starting material similar to our experiments, at similar  $P$ ,  $\Delta T$ ,  $H_2O$  content, and  $f_{O_2}$ . All these cases result in the formation of skeletal-to-dendritic Cpx and minor oxides clustered together. Cpx-Tmt clustering by heterogeneous nucleation may play a fundamental role in the viscosity evolution of a magmatic system, especially in the case of the heterogeneous nucleation of Cpx on Tmt. This clustering mechanism could shorten the nucleation delay typical of magmas at low degrees of undercooling (Arzilli et al. 2019). Moreover, subsequent crystallization of fast-growing dendritic Cpx on already existing Tmt grains may suddenly increase the viscosity of a magma, leading to fragmentation (Moitra et al. 2018) and consequently, basaltic explosive eruption (Arzilli et al. 2019) if the crystallinity remains below 30%. For scenarios with higher undercooling, the result is a higher crystallinity, which can freeze the magma propagation inside dykes or lock crystal mushes in the case of future eruptions (Arzilli et al. 2022). Heterogeneous nucleation of Tmt on Cpx, triggered by rapid formation of skeletal and/or dendritic Cpx, could also have important effects on magmatic systems (Hammer et al. 2010). Cpx crystals decorated or filled with Tmt will have higher density, causing them to be more efficiently removed during settling-related fractional crystallization in melt-rich systems. Furthermore, disequilibrium crystallization of Tmt alongside Cpx should impact the major and trace element signature of coexisting melt in basaltic systems (e.g. Boudreau and Philpotts 2002), and thus also the composition of extracted melt, including in cases where crystallinity is higher and melt extraction proceeds by melt percolation or mush compaction.

## Conclusions

Crystallization experiments and a multi-methodological approach including high resolution 3D SR- $\mu$ CT, EPMA and EBSD mapping provide precious information about the nucleation mechanisms of Tmt and Cpx in a basaltic

melt. The main findings of this work can be summarized as follows:

- 1) Three distinct titanomagnetite (Tmt) populations characterized by different morphologies, sizes, and spatial relations with the other phases formed in a basaltic melt cooled from superliquidus at variable degrees of undercooling ( $\Delta T_{max} - \Delta T_{min} = 100$  °C) along a temperature gradient after applying a single cooling ramp.
- 2) EBSD mapping established the presence of CORs between Tmt and Cpx, which is strong evidence of heterogeneous nucleation of Tmt of populations 2 and 3. The details of the Cpx-Tmt CORs vary between the three Tmt populations, constraining differences in the timing and/or mechanism of nucleation.
- 3) While skeletal Tmt population 1 grains may have nucleated homogeneously from the melt, the other Tmt populations nucleated heterogeneously on Cpx, during and after Cpx crystallization.
- 4) The development of dendritic Cpx morphology and zoning influenced the morphology (and to a lesser extent composition) of Tmt populations 2 and 3, but not the nucleation mechanism, which remained heterogeneous.
- 5) We advise caution when interpreting multiple cooling events to explain differences in crystal morphologies and stress the importance of further study on the presence and proportions of different CORs in experimental and natural samples. This parameter may depend on, and thus provide information about, specific values of undercooling, which are in turn strongly related to the specific crystallisation history of the system.

**Supplementary Information** The online version contains supplementary material available at <https://doi.org/10.1007/s00410-024-02161-w>.

**Acknowledgements** We thank Ilka Wünsche for the sample's preparation, and operator F. Kiraly for the assistance to the FEG-EMPA measurements, carried out at the Department of Lithospheric Research, University of Vienna. EBSD measurements were carried out at the laboratory for field-emission scanning electron microscopy and focused ion beam applications at the Faculty of Geosciences, Geography and Astronomy at the University of Vienna (Austria). We would also like to thank Ralf Dohmen for his comments, suggestions and editing of the manuscript, Fabio Arzilli and an anonymous reviewer for all the precious comments and suggestions that helped improve the manuscript. This research was funded in whole or in part by the Austrian Science Fund (FWF) [Grant DOI: 10.55776/P33227]. For open access purposes, the author has applied a CC BY public copyright license to any author-accepted manuscript version arising from this submission.

**Funding** Open access funding provided by University of Vienna.

**Data availability** Synchrotron 3D reconstructed volumes and unprocessed EBSD data are available from the authors on request; all remaining data can be found in the paper and the supplementary material.

## Declarations

**Competing interests** We declare we have no financial and non-financial interests that are directly or indirectly related to the work submitted for publication.

**Open Access** This article is licensed under a Creative Commons Attribution 4.0 International License, which permits use, sharing, adaptation, distribution and reproduction in any medium or format, as long as you give appropriate credit to the original author(s) and the source, provide a link to the Creative Commons licence, and indicate if changes were made. The images or other third party material in this article are included in the article's Creative Commons licence, unless indicated otherwise in a credit line to the material. If material is not included in the article's Creative Commons licence and your intended use is not permitted by statutory regulation or exceeds the permitted use, you will need to obtain permission directly from the copyright holder. To view a copy of this licence, visit <http://creativecommons.org/licenses/by/4.0/>.

## References

- Ageeva O, Habler G, Pertsev A, Abart R (2017) Fe-Ti oxide microinclusions in clinopyroxene of oceanic gabbro: phase content, orientation relations and petrogenetic implication. *Lithos* 290–291:104–115
- Armienti P, Innocenti F, Petrinì R, Pompilio M, Villari L (1988) Sub-aphyric alkali basalt from Etna: inferences on depth and composition of the source magma. *Rend Soc Ital Min Petrol* 43:877–891
- Armienti P, Perinelli C, Putirka K (2013) A new model to estimate deep-level magma ascent rates, with applications to Mt. Etna (Sicily, Italy). *J Petrol* 45:1–19. <https://doi.org/10.1093/ptrology/egs085>
- Azzilli F, Mancini L, Voltolini M, Cicconi MR, Mohammadi S, Giuli G, Mainprice D, Paris E, Barou F, Carroll MR (2015) Near-Liquid growth of feldspar spherulites in trachytic melts: 3D morphologies and implications in crystallization mechanisms. *Lithos* 216–217:93–105. <https://doi.org/10.1016/j.lithos.2014.12.003>
- Azzilli F, La Spina G, Burton MR, Polacci M, Le Gall N, Hartley ME, Di Genova D, Cai B, Vo NT, Bamber EC, Nonni S, Atwood R, Llewellyn EW, Brooker RA, Mader HM, Lee PD (2019) Magma fragmentation in highly explosive basaltic eruptions induced by rapid crystallization. *Nat Geosci* 12:509–1023–1028. <https://doi.org/10.1038/s41561-019-0468-6>
- Azzilli F, Polacci M, La Spina G, Le Gall N, Llewellyn EW, Brooker RA, Torres-Orozco R, Di Genova D, Neave DA, Hartley ME, Mader HM, Giordano D, Atwood R, Lee PD, Heidelbach F, Burton MR (2022) Dendritic crystallization in hydrous basaltic magmas controls magma mobility within the Earth's crust. *Nat Commun* 13:3354. <https://doi.org/10.1038/s41467-022-30890-8>
- Bachmann O, Huber C (2016) Silicic magma reservoirs in the Earth's crust. *Am Mineral* 101:2377–2404. <https://doi.org/10.2138/am-2016-5675>
- Bachmann O, Dungan MA, Lipman PW (2002) The Fish Canyon magma body, San Juan volcanic field, Colorado: rejuvenation and eruption of an upper crustal batholith. *J Petrol* v 43:1469–1503. <https://doi.org/10.1093/ptrology/43.8.1469>
- Bachmann F, Hielscher R, Schaeben H (2010) Texture analysis with MTEX - free and open source software toolbox. *Solid State Phenom* 160:63–68. <https://doi.org/10.4028/www.scientific.net/SSP.160.63>
- Baddeley A, Rubak E, Turner R (2015) *Spatial Point Patterns: Methodology and Applications with R*. Chapman and Hall/CRC Press. <http://www.crcpress.com/Spatial-Point-Patterns-Methodology-and-Applications-with-R/Baddeley-Rubak-Turner/9781482210200/>
- Bertolett EM, Prior DJ, Gravley DM, Hampton SJ, Kennedy BM (2019) Compacted cumulates revealed by electron backscatter diffraction analysis of plutonic lithics. *Geology* 2019; 47 (5): 445–448. <https://doi.org/10.1130/G45616.1>
- Boudreau A, Philpotts AR (2002) Quantitative modeling of compaction in the Holyoke flood basalt flow, Hartford Basin, Connecticut. *Contrib Mineral Petrol* 144:176–184. <https://doi.org/10.1007/s00410-002-0391-4>
- Brun F, Pacilé S, Kourousias G, Dreossi D, Mancini L, Tromba G, Pugliese R (2015) Enhanced and flexible software tools for X-ray tomography experiments at the Italian synchrotron radiation facility Elettra. *Fundamenta Informaticae* 141:233–243. <https://doi.org/10.3233/FI-2015-1273>
- Cashman KV, Sparks RSJ, Blundy JD (2017) Vertically extensive and unstable magmatic systems: a unified view of igneous processes. *Science* 355:eaag3055. <https://doi.org/10.1126/science.aag3055>
- Colle F, Masotta M, Costa S, Mollo S, Landi P, Pontesilli A, Peres S, Mancini L (2023) Effect of undercooling on clinopyroxene crystallization in a high K basalt: implications for magma dynamics at Stromboli volcano. *Lithos* Volumes 456–457. <https://doi.org/10.1016/j.lithos.2023.107327>
- Costa S, Masotta M, Gioncada A, Pistolesi M, Bosch D, Scarlato P (2020) Magma evolution at La Fossa volcano (Vulcano Island, Italy) in the last 1000 years: evidence from eruptive products and temperature gradient experiments. *Contrib Mineral Petrol* 175:31. <https://doi.org/10.1007/s00410-020-1669-0>
- R Core Team (2020) R: A language and environment for statistical computing. R Foundation for Statistical Computing, Vienna, Austria. <https://www.R-project.org/>
- DiBenedetto M, Qin Z, Suckale J (2020) Crystal aggregates record the pre-eruptive flow field in the volcanic conduit at Kīlauea, Hawaii: science advances, v. 6. eabd4850. <https://doi.org/10.1126/sciadv.abd4850>
- Dowty E (1980) Synneusis Reconsidered. *Contr. Mineral. and Petrol.* 74, 75–84 (1980). <https://doi.org/10.1007/BF00375491>
- Dyck B (2023) Sticking together: mechanisms of quartz synneusis in high-silica magma. *Geosci Front* 14(2023):101512. <https://doi.org/10.1016/j.gsf.2022.101512>
- Dyck B, Holness M (2021) Microstructural evidence for convection in high-silica granite. *Geology* 50:295–299. <https://doi.org/10.1130/G49431.1>
- Ellis BS, Bachmann O, Wolff JA (2014) Cumulate fragments in silicic ignimbrites: the case of the Snake River Plain. *Geology* 42:431–434. <https://doi.org/10.1130/G35399.1>
- Feinberg JM, Wenk HR, Renne PR, Scott GR (2004) Epitaxial relationships of clinopyroxene-hosted magnetite determined using electron backscatter diffraction (EBSD) technique. *Am Mineral* 89:462–466
- Ferguson MRM, Ehrig K, Meffre S (2019) Insights into magma histories through silicate-oxide crystal clusters: linking the Hiltaba Suite intrusive rocks to the Gawler Range Volcanics, Gawler Craton, South Australia. *Precambrian Res* 321:103–122. <https://doi.org/10.1016/j.precamres.2018.11.015>
- Ferracutti GR, Gargiulo MF, Ganuza ML (2015) Determination of the spinel group end-members based on electron microprobe analyses. *Miner Petrol* 109:153–160 (2015). <https://doi.org/10.1007/s00710-014-0363-1>
- Fleet ME, Bilcox GA, Bennett RL (1980) Oriented magnetite inclusions in pyroxenes from the Greenville Province. *Can Mineral* 18:89–99
- Freda C, Gaeta M, Misiti V, Mollo S, Dolfi D, Scarlato P (2008) Magma-carbonate interaction: an experimental study on

- ultrapotassic rocks from Alban Hills (Central Italy). *Lithos* 101:397–415. <https://doi.org/10.1016/j.lithos.2007.08.008>
- Garcia MO, Jacobson SS (1979) Crystal clots, amphibole fractionation and the evolution of calc-alkaline magmas. *Contrib Mineral Petrol* 69:319–327. <https://doi.org/10.1007/BF00372257>
- Gordon C, Wallis D (2024) Resolving the megacryst paradox: Feldspar orientation relationships record crystal mobility in granites. *Geology* 2024; <https://doi.org/10.1130/G52045.1>
- Habler G, Griffiths TA (2017) Crystallographic orientation relationships. In: *Mineral reaction kinetics: Microstructures, textures, chemical and isotopic signatures*. pp 541–585
- Hammer JE (2008) experimental Studies of the Kinetics and energetics of Magma Crystallization. *Minerals, Inclusions and Volcanic Processes* pp 9–59
- Hammer JE, Sharp TG, Wessel P (2010) Heterogeneous nucleation and epitaxial crystal growth of magmatic minerals. *Geology* 38:367–370. <https://doi.org/10.1130/G30601.1>
- Hielscher R, Schaeben H, Siemes H (2010) Orientation distribution within a single Hematite Crystal. *Math Geosci* 42:359–375. <https://doi.org/10.1007/s11004-010-9271-z>
- Holness MB, Farr R, Neufeld JA (2017) Crystal settling and convection in the Shiant isles Main Sill. *Contrib Mineral Petrol* 172:7. <https://doi.org/10.1007/s00410-016-1325-x>
- Holness MB, Stock MJ, Geist D (2019) Magma chambers versus mush zones: constraining the architecture of sub-volcanic plumbing systems from microstructural analysis of crystalline enclaves. *Philos Trans R Soc Lond* 377:20180006. <https://doi.org/10.1098/rsta.2018.0006>
- Holness MB, Vukmanovic Z, O'Driscoll B (2023) The formation of Chromite chains and clusters in Igneous Rocks. *J Petrol* 64:1–24. <https://doi.org/10.1093/petrology/egac124>
- Jerram DA, Cheadle MJ (2000) On the cluster analysis of grains and crystals in rocks. *Am Min* 85(1):47–67. <https://doi.org/10.2138/am-2000-0107>
- Jerram DA, Cheadle MJ, Philpotts AR (2003) Quantifying the Building blocks of Igneous rocks: are clustered Crystal frameworks the Foundation? *J Petrol* 44:2033–2051. <https://doi.org/10.1093/petrology/egg069>
- Kilauea, Volcano, Hawaii GSA Bull 88:78–84. [https://doi.org/10.1130/0016-7606\(1977\)88%3C78:NAGOPM>2.0.CO;2](https://doi.org/10.1130/0016-7606(1977)88%3C78:NAGOPM>2.0.CO;2)
- Kirkpatrick RJ (1977) Nucleation and growth of plagioclase. *Makopuhi and Alae lava lakes*
- Kirkpatrick RJ (1981) Kinetics of crystallization of igneous rocks. In *Rev. Mineral., Vol. 8* (eds. A. C. Lasaga and R. J. Kirkpatrick), pp. 321–395
- Lindsley DH, Andersen DJ (1983) A two-pyroxene thermometer. *J Geophys Res Solid Earth* 88:A887–A906. <https://doi.org/10.1029/JB088iS02p0A887>
- Lofgren GE (1983) Effect of heterogeneous nucleation on basaltic textures: a dynamic crystallization study. *J Petrol* 24:229–255. <https://doi.org/10.1093/petrology/24.3.229>
- Marsh BD (2002) On bimodal differentiation by solidification front instability in basaltic magmas: Part I. Basic mechanics. *Geochim. Cosmochim Acta* 66:2211–2229
- Masotta M, Freda C, Paul TA, Moore GM, Gaeta M, Scarlato P, Troll VR (2012a) Low pressure experiments in piston cylinder apparatus: calibration of newly designed 25 mm furnace assemblies to P=150 MPa. *Chem Geol* 312:74–79. <https://doi.org/10.1016/j.chemgeo.2012.04.011>
- Masotta M, Freda C, Gaeta M (2012b) Origin of crystal-poor, differentiated magmas: insights from thermal gradient experiments. *Contrib Miner Petrol* 163(1):49–65
- Masotta M, Pontesilli A, Mollo S, Armienti P, Ubide T, Nazzari M, Scarlato P (2020) The role of undercooling during clinopyroxene growth in trachybasaltic magmas: insights on magma decompression and cooling at Mt. Etna volcano. *Geochim. Cosmochim Acta* 268:258–276. <https://doi.org/10.1016/j.gca.2019.10.009>
- Moitra P, Gonnermann HM, Houghton BF, Tiwary CS (2018) Fragmentation and plinian eruption of crystallizing basaltic magma. *Earth Planet Sci Lett* v 500:97–104. <https://doi.org/10.1016/j.epsl.2018.08.003>
- Mollo S, Del Gaudio P, Ventura G, Iezzi G, Scarlato P (2010) Dependence of clinopyroxene composition on cooling rate in basaltic magmas: implications for thermobarometry. *Lithos* 118:302–312
- Mollo S, Iezzi G, Ventura G, Cavallo A, Scarlato P (2012) Heterogeneous nucleation mechanisms and formation of metastable phase assemblages induced by different crystalline seeds in a rapidly cooled andesitic melt. *J Non Cryst Solids* 358:1624–1628
- Mollo S, Putirka K, Iezzi G, Scarlato P (2013) The control of cooling rate on titanomagnetite composition: implications for a geospeedometry model applicable to alkaline rocks from Mt. Etna volcano. *Contrib Mineral Petrol* 165:457–475. <https://doi.org/10.1007/s00410-012-0817-6>
- Paganin D, Mayo SC, Gureyev TE, Miller PR, Wilkins SW (2002) Simultaneous phase and amplitude extraction from a single defocused image of a homogeneous object. *J Microsc* 206:33–40. <https://doi.org/10.1046/j.1365-2818.2002.01010.x>
- Polacci M, Mancini L, Baker DR (2010) The contribution of synchrotron X-ray computed microtomography to understanding volcanic processes. *J Synchrotron Rad* 17:215–221
- Pontesilli A, Masotta M, Nazzari M, Mollo S, Armienti P, Scarlato P, Brenna M (2019) Crystallization kinetics of clinopyroxene and titanomagnetite growing from a trachybasaltic melt: new insights from isothermal time-series experiments. *Chem Geol* 510:113–129. <https://doi.org/10.1016/j.chemgeo.2019.02.015>
- Ripley BD (1976) The second-order analysis of stationary point processes. *J Appl Probab* 13:255–266
- Ripley BD (1977) Modelling spatial patterns. *J R Stat Soc B* 39:172–192
- Rudge JF, Holness MB, Smith GC (2008) Quantitative textural analysis of packings of elongate crystals. *Contrib Mineral Petrol* 156:413–429. <https://doi.org/10.1007/s00410-008-0293-1>
- Schindelin J, Arganda-Carreras I, Frise E, Kaynig V, Longair M, Pietzsch T, Preibisch S, Rueden C, Saalfeld S, Schmid B, Tinevez J-Y, White DJ, Hartenstein V, Eliceiri K, Tomancak P, Cardona A (2012) Fiji: an open-source platform for biological-image analysis. *Nat Methods* 9:676–682
- Schwindinger KR (1999) Particle dynamics and aggregation of crystals in a magma chamber with application to Kilauea Iki olivines. *J Volcanol Geotherm Res* 88:209–238. [https://doi.org/10.1016/S03770273\(99\)00009-8](https://doi.org/10.1016/S03770273(99)00009-8)
- Schwindinger KR, Anderson AT (1989) Synneusis of Kilauea Iki olivines. *Contrib Mineral Petrol* 103:187–198. <https://doi.org/10.1007/BF00378504>
- Shea T, Hammer JE (2013) Kinetics of decompression and cooling-induced crystallization of mafic-intermediate hydrous magmas. *J Volcanol Geotherm Res* 260:127–145
- Stoyan D, Stoyan H (1994) *Fractals, Random Shapes and Point Fields. Methods of Geometrical Statistics. XIV*, 389 pp. John Wiley & Sons 1994
- Sunagawa I (1981) Characteristics of crystal growth in nature as seen from the morphology of mineral crystals. *Bull Min* 104:81–87
- Vance JA (1969) On synneusis. *Contrib Mineral Petrol* 24:7–29. <https://doi.org/10.1007/BF00398750>
- Vetere F, Iezzi G, Behrens H, Holtz F, Ventura G, Misiti V, Cavallo A, Mollo S, Dietrich M (2015) Glass forming ability and crystallisation behaviour of sub-alkaline silicate melts. *Earth-Sci Rev* 150:25–44. <https://doi.org/10.1016/j.earscirev.2015.07.001>
- Vukmanovic Z, Holness MB, Monks K (2018) The Skaergaard trough layering: sedimentation in a convecting magma chamber.



- Contrib Mineral Petrol 173, 43 (2018). <https://doi.org/10.1007/s00410-018-1466-1>
- Walker D, Kirkpatrick RJ, Longhi J, Hays JF (1976) Crystallization history of lunar picritic basalt samples 12002: phase equilibria and cooling rate studies. *Geol Soc Am Bull* 87:646–656
- Wieser PE, Vukmanovic Z, Kilian R, Ringe E, Holness MB, Maclennan J, Edmonds E (2019) To sink, swim, twin, or nucleate: a critical appraisal of crystal aggregation processes. *Geology* 47:948–952. <https://doi.org/10.1130/G46660.1>
- Zandomenghi D, Voltolini M, Mancini L, Brun F, Dreossi D, Polacci M (2010) Quantitative analysis of X-ray microtomography images of geomaterials: application to volcanic rocks, *Geosphere*. 6:793–804. <https://doi.org/10.1130/GES00561.1>

**Publisher's Note** Springer Nature remains neutral with regard to jurisdictional claims in published maps and institutional affiliations.